Friedrich-Alexander-Universität
Erlangen-Nürnberg

Master's Thesis in Physics

XMM-Newton Analysis of SNR J0506-7009

Edwin John Anthikat

Supervised by:
Prof. Dr. Manami Sasaki

Dr. Karl-Remeis Sterwarte, Bamberg
Friedrich-Alexander-Universität Erlangen-Nürnberg

January 2026

Abstract

Aims. I study the diffuse X-ray emission observed in the field of view of the supernova remnant (SNR) J0506–7009 in the Large Magellanic Cloud (LMC) by *XMM-Newton*. I want to understand the nature of this soft diffuse emission and learn the origin and properties of the SNR in the study. I also investigate the nature of a dense region near the SNR, seen in the optical images.

Methods. I analysed the *XMM-Newton* spectra of the diffuse emission of the SNR. An X-Ray-loud center is seen in a faint optical shell. The data were processed using XMM-ESAS and fit using XSPEC. Further, MCELS, MAGMA and H I Parkes All-Sky Survey were used to get a better understanding of the SNR and the dense clouds in the immediate environment.

Results. The analysis of the spectra shows that the soft X-ray emission arises from the hot gas of an old SNR. The central emission has a spectrum dominated in the medium energy band ($700 - 1100$ eV), with the deduced Fe abundance in excess of solar and not consistent with the LMC abundance. A standard Sedov analysis implies an SNR age of ~ 41000 years. The type of the supernova explosion could not be determined conclusively. There is a molecular cloud complex and an H α region with spatial correlation with the SNR. The initial mass function reveals 3 massive stars in the latter region, of which one is still active. The H I map shows no cavity and thus negates the possibility of this region being an H II region.

Contents

CHAPTER 1

Introduction

Most stars explode at the end of their lives. Such stellar explosions known as supernovae expel stellar material and drive shock waves into the interstellar medium (ISM). These explosions are extremely luminous and can outshine an entire galaxy. What this big event does to the surrounding medium remains long after the event as a structure known as a supernova remnant (SNR). This remnant contains accounts of where and how the explosion occurred (Dang et al. [2024]). Therefore, motivated to find the origin and evolution of SNR J0506-7009, an SNR located in the LMC, the x-ray emission of this region is analysed and studied in this thesis. The host galaxy, the Large Magellanic Cloud, is an irregular dwarf galaxy, which has been the subject of extensive research on SNRs since their initial scientific detection by Mathewson and Healey [1964] and holds significant interest in the search for SNRs because it is nearly face-on to our position in the universe (Delmotte [2004]), it has low foreground absorption and is relatively close, at a distance of 50 kpc (Pietrzyński et al. [2019]).

The motivation of supernova (SN) studies goes far beyond curiosity about a single object because supernova remnants are vessels of the past, holding tales of ages. Supernova studies offer valuable insights into both the stars that preceded these dramatic events and the environments in which they occur. By analysing the spectra of the remnants, we can deduce the distribution and composition of the surrounding interstellar medium (ISM) and trace the material ejected by the progenitor star. This analysis allows us to reconstruct the progenitor's characteristics at the time of its demise and, for example, provides a crucial testbed for models of stellar evolution. The detection of neutrinos from SN 1987A in the LMC offered compelling confirmation of core-collapse supernova models, lending significant weight to the theoretical framework. Brakenridge [2025] studies SNRs near Earth and speculates how supernovae may have affected Earth's atmosphere during the late quaternary.

The next three chapters will introduce the physics needed to understand this thesis, then Chapter 5 will present the data processing and methods of X-ray spectral analysis along with introducing other data used in this thesis, and then the results will be presented and discussed in chapters 6 and 7.

CHAPTER 2

Star: Formation and Evolution

A star is a body bound by self-gravity, radiating energy from an internal source (Prialnik [2009]). Thus, a star is born when a body of gas fulfills these two conditions and is dead when either of these is broken. This chapter will introduce how these conditions are fulfilled and broken as well the internal source of energy.

2.1 Interstellar Medium

While stars appear to be in just empty space for naked eyes, they are immersed in a medium of gas and dust, the interstellar medium (ISM); as explained in Prialnik [2009]. This pervasive medium, primarily composed of gas and dust, constitutes a significant fraction of a galaxy's baryonic mass. In the Milky Way, the ISM accounts for approximately a few percent ($\sim 10^9 \text{M}_\odot$) of the total galactic mass, predominantly confined to a thin disk with a thickness of less than 10^3 light-years and a diameter of $\sim 10^5$ light-years, concentrated around the galactic midplane. Despite its galactic-scale distribution, the average particle number density within the ISM is exceedingly low, on the order of one particle per cubic centimeter, corresponding to a mass density of $\sim 10^{-21}$kg m^{-3}.

The dominant elemental constituent of the galactic gas, serving as the primordial material for star formation, is hydrogen, comprising approximately 70% of the ISM's mass. This hydrogen exists in various forms depending on the local physical conditions: molecular hydrogen (H_2), neutral atomic hydrogen (H I), and ionized hydrogen (H II). Helium constitutes the majority of the remaining mass. The distribution of interstellar material is far from uniform; instead, it is organized into discrete structures known as nebulae, which are localized enhancements in gas and dust density. While some nebulae, such as planetary nebulae, supernova remnants, and nova shells, represent transient phases of stellar evolution, their eventual dissipation contributes to the broader ISM, enriching it with processed material. The ISM exhibits a wide range of densities, from relatively dense clouds with number densities reaching thousands of particles per cubic centimeter to a more diffuse intercloud medium with densities significantly below one particle per cubic centimeter.

The ISM also contains giant molecular clouds, characterized by high densities ($1 - 3 \times 10^8$ m^{-3} and higher), low temperatures (as low as 10 K), significant dust content, and substantial masses (up to 10^6 M$_\odot$) spanning approximately 100 light-years. These dense, cold molecular clouds are the primary sites of star formation within galaxies.

2.2 Molecular Clouds

Molecular clouds are interstellar clouds of gas and dust in which molecules can form (Buhl [1973]). There are many academic uncertainties about a molecular cloud, including their definition (Chevance et al. [2020]) and lifetime (Hygate [2020]). Theoretical models suggest that molecular clouds are the largest structures in galaxies that can become self-gravitating and evolve independently of galactic dynamics, driven mainly by internal physics. This is supported by recent observational findings, which indicate that these clouds represent fundamental, independently evolving units that determine how stars form within galaxies (Chevance et al. [2020] and references therein).

Molecular clouds exhibit a complex hierarchical structure, often appearing as dense clumps and filaments on all scales embedded within a more diffuse envelope (Klessen et al. [1998]). Turbulence plays a crucial role in shaping this structure, creating density fluctuations that can eventually lead to gravitational fragmentation where the large, unstable mass of gas breaks apart into numerous smaller, denser pieces or fragments, each with the potential to further collapse and form individual stars or multiple star systems. Fragmentation starts with the dissipation of small-scale features by pressure, while the large-scale fluctuations start to collapse onto themselves and into filaments and knots. Subsequently, these dense regions, known as cores, collapse under self-gravitation when they exceed the Jeans mass, a critical mass at which the inward force of gravitation overcomes the outward pressure. Stars form within these cores of giant molecular clouds (GMCs) that have abundant molecular hydrogen (Prialnik [2009]).

GMCs are not static entities, but rather dynamic structures that undergo a continuous cycle of evolution. This lifecycle can be broadly divided into three key phases, each characterized by distinct physical processes and open questions. The first phase involves the assembly of GMCs from a more diffuse interstellar medium. This tenuous material can exist in either atomic or molecular form, a state determined by the midplane gas pressure of the host galaxy. GMC formation can be triggered by various mechanisms, including gravitational instability, turbulent motion, and large-scale shocks. A central question in this phase is understanding how these formation mechanisms vary depending on the galactic environment. Once formed, GMCs enter a period of star formation. Within these clouds, the densest regions, under the influence of their own gravity, begin to decouple from the turbulent flow. This leads to the collapse of these regions and the subsequent birth of stars. However, the efficiency of this process, with only about 1% of the cloud's mass converted into stars per cloud-scale free-fall time, remains a significant puzzle. Chevance et al. [2020] describes two scenarios to explain the low Star Formation Efficiency (SFE) and Star Formation Rate (SFR) in molecular clouds: (i) slow and efficient, (ii) fast and inefficient. Magnetohydrodynamics play a significant role in slowing down star formation. Weaker magnetic support enhances the efficiency of star formation, resulting in the formation of star clusters. If the star formation is quick, the stellar feedback mechanisms can disrupt the cloud. Early disruption of a star-forming cloud leads to inefficient conversion of gas into stars. The final phase of a GMC's life is its dispersal. The ultimate fate of a GMC is heavily dependent on the characteristics of the stars it forms. If the GMC gives rise to massive stars, their photodissociating radiation, powerful stellar winds, and eventual supernova explosions can disrupt and disperse the cloud. In this scenario, the dominant feedback mechanism responsible for this dispersal is the main question. Alternatively, if the GMC primarily forms low-mass stars, its dispersal may be driven by more gradual processes, such as local galactic dynamics or galactic shear, particularly if the cloud is not gravitationally bound (Chevance et al. [2020]).

In addition to gravitationally bound MCs, less denser molecular gas is also found in galaxies. 99% of molecular gas is H_2. However, no permanent dipole moment and cold temperatures make it almost impossible to observe directly. The alternate approach is to probe with other molecules, commonly carbon monoxide (CO). CO is the second most abundant interstellar molecule after molecular hydrogen (Saberi et al. [2019]). Every molecular cloud will have CO emission. For this detection, the J = $1-0$ transition line of CO at 115 GHz is the best match with the higher optical thickness of the ^{12}CO($1-0$) line and the low gas density needed to excite this line (Dame et al. [2001]). Moreover, the photodissociation boundaries are closer for CO and H_2 (Saberi et al. [2019]) and, generally, for each gas clump the observed CO line intensity is proportional to the molecular gas mass and the conversion requires only the use of a conversion factor X_{CO} (Narayanan et al. [2012]). With lower metallicity than our galaxy, X_{CO} for LMC is larger than that of the Milky Way (Israel [1997]; Lebouteiller et al. [2019]).

Stars form in MCs and then can slowly drift away. Long living stars can thus be found farther away from their parent clouds than short living stars. Low mass stars tend to live longer than high mass stars. Therefore, a simple inference can be made, that the high mass stars and hence their SNRs can be found near the parent MCs (Makarenko et al. [2023]). Huang and Thaddeus [1986] studies 26 outer Galaxy SNRs and concludes that roughly half of them are found near molecular cloud complexes. The study notes the statistical improbability of a spatial coincidence resulting from a superposition. Spatial correlation is the evidence commonly used to claim SNR-MC associations (Zhou et al. [2023]). An SNR can shape the neighboring MCs (Jiang et al. [2010]).

The H.E.S.S. Collaboration (Aharonian et al. [2008]) detects TeV γ-ray emission from the W28 region coincident with molecular clouds. This emission is commonly explained by the hadrons accelerated in the shock of a supernova remnant interacting with the nearby MCs after escaping the shock front. The proton-proton interaction here followed by the pion decay produces the γ-ray emission. Abdo et al. [2010] detects the γ-ray emission from the W28 region in the GeV regime. Thus, high-energy cosmic rays can be traced to MC-SNR associations.

As we saw earlier, stars form in the GMCs. The minimum Jeans mass is ~ 0.003 $M_\odot$ and the maximum ~ 0.1 $M_\odot$ (Forgan and Rice [2011]), and the lower stellar mass limit is 0.08 $M_\odot$. That is, the minimum Jeans mass is about an order of magnitude lower than the lower stellar mass limit. Therefore, not everything that is formed in these cores becomes a star, some end up as brown dwarfs. Brown dwarfs dim and cool with age, but stars become brighter and hotter with age.

2.3 Stars

The collapsing cloud that will later become a star is now, at this point in its evolution, called a protostar. As the protostar shrinks, it spins faster, conserving angular momentum. This spin flattens the surrounding material into a rotating disk, known as an accretion disk, which feeds material onto the growing protostar. Eventually, the core of the protostar becomes hot and dense enough to ignite nuclear fusion. The primary fusion process is hydrogen fusion, where hydrogen atoms fuse to form helium, releasing tremendous amounts of energy in the process. This energy creates an outward pressure that balances the inward pull of gravity, establishing a state of hydrostatic equilibrium. At this point, the protostar is officially born as a star, and it enters the main sequence phase of its life.

A star spends the majority of its life in the main sequence, steadily fusing hydrogen into helium in its core. The star's position on the main sequence is determined primarily by its mass. Massive stars are hotter, brighter, and have shorter lives, while low-mass stars are cooler, fainter, and live much longer. Our Sun, a low mass star, has been in the main sequence for about 4.6 billion years and is expected to remain there for another 5 billion years. During this stable period, the star's size, luminosity, and temperature remain relatively constant.

As the star continues to burn hydrogen, the core gradually accumulates helium. Eventually, the hydrogen fuel in the core is exhausted. What happens next depends critically on the star's mass.

For stars like our Sun, with masses less than about 8 times the mass of the Sun, the end of the main sequence marks the beginning of a series of dramatic transformations. With no hydrogen left in its core, the core begins to contract under its own gravity. However, hydrogen fusion continues in a shell surrounding the core. The contracting core heats up, causing the outer layers of the star to expand dramatically. The star becomes a red giant, a bloated, cooler star, hundreds of times larger than its original size. As the core continues to contract, it eventually becomes hot enough to ignite helium fusion, where helium fuses into carbon and oxygen. This phase is relatively short-lived.

Eventually, the helium fuel in the core is also exhausted. The star, now with a carbon-oxygen core, is unable to reach the temperatures required for further fusion. The outer layers of the star are gently ejected into space, forming a beautiful, expanding shell of gas called a planetary nebula. The exposed core, now composed primarily of carbon and oxygen, is extremely hot and dense. It no longer undergoes fusion, but it continues to radiate heat. This stellar remnant is called a white dwarf. Electron-degeneracy pressure prevents the white dwarf from collapsing further. They slowly cool and fade over billions of years, eventually becoming a cold, dark remnant.

Stars significantly more massive than the Sun ($>\sim 8$ $\mathrm{M}_\odot$) follow a much more dramatic and violent path at the end of their lives. They evolve into red supergiants. These massive stars have enough gravity to compress their cores to temperatures and densities high enough to fuse helium into carbon and oxygen, and then carbon and oxygen into even heavier elements, such as neon, silicon, and finally iron. Iron is the end of the line for nuclear fusion in stars. The fusion of iron does not release energy; instead, it consumes energy. At this point, the core can no longer oppose the immense inward gravitational force. The core collapses catastrophically in a fraction of a second, an event known as supernova. Low mass stars can also end up in SNe. These mechanisms are detailed in the next section.

2.4 Supernovae

A supernova (SN) is an enormous explosion at the end of a star's life caused by the instability of the collapsing core. This explosion releases a huge amount of energy ($\sim 10^{53}$ erg). During the supernova, elements heavier than iron, such as gold, silver, and uranium, are synthesized in a process called nucleosynthesis. The outer layers of the star are blasted into space at incredible speeds, enriching the interstellar medium with these heavy elements. Supernovae can also induce star formation by compressing cold clumps of the ISM and leading to their gravitational collapse.

Supernovae can be classified into different groups based on their spectra and light curves, mainly into type I SNe and type II SNe, and then further into different subgroups. Hydrogen lines are absent in the former and present in the latter. By the nature of their formation, SNe can be separated into thermonuclear or type Ia, formed by the thermonuclear explosion of a white dwarf, or as core-collapse (CC) SNe, formed by the collapse of the stellar core. These two types of SNe are discussed here, based on Seward and Charles [2010] and Vink [2012].

A white dwarf survived an explosion because its mass was less than the Chandrasekhar limit (1.4 $\mathrm{M}_\odot$), where the degenerate electron pressure stabilized the inward gravitational collapse. However, this white dwarf can increase its mass by merging with another white dwarf or by accreting mass from a star or brown dwarf and reach a point where the inward force dominates. The subsequent increase in temperature facilitates C/O burning, and the resulting energy disrupts the white dwarf, exploding as a type Ia SN. Type Ia supernovae are observed in all types of galaxies, including older ones and galactic halos, where star formation is absent. This suggests that their progenitors are old, less massive stars that have already lost their hydrogen envelopes during their evolution, corroborating the classification criterion of the absence of spectral hydrogen lines.

However, CC SNe are observed almost exclusively in the arms of spiral galaxies and in irregular galaxies. These are two places of star formation. Therefore, CC SNe are believed to have young progenitors. The core collapse of a massive star (> 8 M $_{\odot}$) is assumed to cause a CC SNe. The light curves of the two types of SNe are significantly different. The light curves of type Ia SNe have a sharp maximum with luminosities of the order of 10^9 $L_{\odot}$, followed by a quick exponential decay that flattens with time. Whereas, the maxima of the CC SNe are broader and lower, followed by an exponential decay. While the light curves of all type Ia SNe are similar, owing to the quick ignition at the same mass limit, the light curves of CC SNe can differ from one SN to the other. Therefore, as the light curves are influenced by the initial stellar mass and the evolutionary stage, CC SNe are assumed to happen from different types of progenitors.

The elementary compositions of these two types of SNe are also significantly different. Obviously, massive progenitor stars of CC SNe can fuse nuclei up to Fe with the highest binding energy. When these iron nuclei form a degenerate core, the Si burning continues in a shell around this core, adding more Fe to the core, thereby increasing the core mass. Thus, the core crosses the Chandrasekhar limit and the degeneracy pressure of the electrons can no longer stabilize the core against gravity. Thereafter, the core contracts, increasing the temperature. At these higher temperatures, the iron decomposes into lighter nuclei. However, in type Ia SNe where the the progenitor white dwarfs have mostly carbon and oxygen, the explosion creates radioactive ^{56}Ni. The radioactive decay of ^{56}Ni synthesizes iron. Therefore, type Ia SNe will have more iron compared to lighter elements, while CC SNe will have more lighter elements than iron. This trend in abundance is a significant probe in identifying the type of explosion from a remnant of the SN.

The fate of the core collapsed in the supernova depends on its mass. If the core's mass is between about 1.4 and 3 solar masses, the core collapses into a highly dense object called a neutron star. Neutron stars are composed almost entirely of neutrons, packed together so tightly that a teaspoonful of neutron star material would weigh billions of tons on Earth. They spin rapidly and have intense magnetic fields, sometimes emitting beams of radiation that we detect as pulsars. If the core's mass is greater than about 3 solar masses, even neutron degeneracy pressure cannot prevent further collapse. The core continues to collapse until it forms a singularity, a point of infinite density. The gravity of this singularity is so strong that nothing, not even light, can escape. This object is called a black hole.

Additionally, there has been another type of SN theorized, called Pair Instability (PI) SN. These are explosions of highly massive (140-260 $M_{\odot}$) stars whose cores contract as the outward pressure from the core decreases due to pair production as a result of high-energy gamma rays interacting with the nuclei of the core (Chen et al. [2014]). Here, as the core temperature and density increases steeply, explosive burning of oxygen and silicon is triggered, releasing energy up to 10^{53} erg. This explosion completely unbinds the star, and as opposed to other SN explosions, no compact object is left behind. Whalen et al. [2025] shows how these cores could have harbored the first water in the universe; $100 - 200$ Myr after the big bang.

While the supernova explosion itself can only be visible for a few weeks, the remainder of this extremely powerful explosion has a shocking effect on the ambient medium that this remainder can exist for up to ~ 100000 years. This remainder, which is the ejecta of the explosion and the ISM swept up by the shock front, is a structure known as a supernova remnant.

2.5 Supernova Remnants

SNRs are the structures formed from the material ejected during a supernova explosion and its interaction with the surrounding ISM.

Following the explosive death of massive stars or the thermonuclear detonation of white dwarfs, SNRs evolve through distinct phases, each characterised by unique physical processes. Supernova explosions, whether core-collapse or Type Ia, release vast amounts of energy, typically on the order of 10^{51} erg, propelling stellar material into the surrounding ISM at velocities exceeding $10,000$ km/s. This ejected material, enriched with heavy elements synthesized during the star's life and the explosion, forms the initial structure of an SNR. Ackermann et al. [2013], Giuliani and AGILE Team [2011] etc. shows how SNRs accelerate cosmic rays to $\sim 10-100$ TeV and Sushch et al. [2025] shows how SNRs can accelerate cosmic rays to PeV ranges in extreme conditions. The interaction between the high-velocity ejecta and the ambient ISM generates shock waves, which heat and compress the surrounding gas, creating a dynamic and evolving system. The initial conditions, such as the progenitor star's mass, the explosion mechanism, and the density of the surrounding ISM, significantly influence the SNR's subsequent evolution. The evolution of SNRs is typically divided into four stages: the free-expansion phase, the Sedov-Taylor phase, the radiative phase, and the merging phase. Each stage is governed by distinct physical processes and timescales, influenced by the explosion energy, ejecta mass, and ISM density.

In the free-expansion phase, the ejecta travel at nearly constant velocity, unimpeded by the surrounding ISM. This phase lasts until the swept-up mass from the ISM becomes comparable to the ejecta mass, typically a few hundred years. The shock front moves supersonically, heating the ISM to temperatures of 10^6–10^8 K, producing X-ray emission observable by telescopes like Chandra and XMM-Newton. The remnant's radius grows linearly with time, approximated as $R \propto t$.

As the swept-up mass exceeds the ejecta mass, the SNR enters the Sedov-Taylor phase, characterized by adiabatic expansion. The shock front decelerates, and the remnant's evolution is described by the self-similar Sedov-Taylor solution, where the radius scales as $R \propto t^{2/5}$. The hot interior, with temperatures around 10^7 K, emits X-rays, while the shock continues to sweep up ISM material. This phase, lasting several thousand years, is critical for studying the energy transfer from the supernova to the ISM.

As the shock velocity decreases below approximately 200 km/s, radiative losses become significant, marking the transition to the radiative phase. The shocked gas cools, forming a dense shell that emits strongly in optical and ultraviolet wavelengths. Forbidden lines, such as [O III] and [S II], dominate the spectra, providing insights into the chemical composition and ionization state of the remnant. The radius evolves as $R \propto t^{1/4}$, and this phase can last tens of thousands of years, depending on the ambient density.

In the final stage, the SNR's shock velocity approaches the ISM's turbulent velocity, typically 10–20 km/s. The remnant loses its distinct structure, blending into the ISM. This phase, which can last hundreds of thousands of years, marks the dispersal of the SNR's energy and enriched material into the galactic environment, influencing future star formation and ISM dynamics.

The interaction also drives turbulence in the ISM, contributing to its multiphase structure. Hot, ionized gas from the SNR interior coexists with cooler, neutral regions, creating a complex interplay of thermal and magnetic pressures. Magnetic fields, amplified by shock compression, play a role in confining cosmic rays accelerated within SNRs, which further influence ISM dynamics.

SNRs are observed across the electromagnetic spectrum, each wavelength revealing distinct physical processes. In X-rays, the hot plasma in the Sedov-Taylor phase produces thermal bremsstrahlung and line emission, allowing astronomers to probe temperature, density, and composition. Optical observations reveal filamentary structures in the radiative phase, with emission lines providing diagnostics of shock velocity and ionization. Radio emission, primarily synchrotron radiation from relativistic electrons, indicates cosmic ray acceleration and magnetic field amplification (Onić et al. [2012]). Recent advances in multiwavelength observations, combined with numerical simulations, have enhanced our understanding of SNR evolution. For instance, the Atacama Large Millimeter/submillimeter Array (ALMA) has detected molecular emission from SNRs, revealing interactions with dense molecular clouds(Sano et al. [2021]).

While SNRs are the direct outcome of one SN explosion, the extreme explosive energies of multiple explosions can create cavities in the ISM, known as superbubbles. Unlike individual supernova remnants where the energy input is instantaneous, superbubbles result from the cumulative energy injection over millions of years, creating large-scale structures that significantly impact galactic dynamics.

2.6 Superbubbles

Superbubbles are expansive, hot cavities in the ISM, typically spanning hundreds of parsecs, formed by the combined effects of multiple supernova explosions and stellar winds from massive stars in OB associations or star clusters.

Superbubbles originate in regions of active star formation, where massive stars ($M > 8\ M_{\odot}$) form in clusters. The overlapping shock waves from the SN events coalesce, forming a single, expanding cavity surrounded by a dense shell of swept-up ISM material. The energy input, often exceeding 10^{53} erg over the lifetime of the star cluster, inflates the superbubble, creating a low-density, high-temperature interior with temperatures of 10^6–10^8 K. The initial conditions, including the number of massive stars, the ambient ISM density, and the magnetic field strength, govern the size and evolution of the superbubble. In dense star-forming regions, such as those in spiral arms, superbubbles can grow to diameters of 100–1000 pc, reshaping the surrounding ISM.

While superbubbles carve out vast, hot regions through mechanical energy, H II regions, in contrast, are primarily shaped by the intense ionising radiation emitted by massive stars, creating glowing, ionised nebulae within or near these same star-forming environments.

2.7 H II Region

Hot massive stars radiate ultraviolet radiations that photoionise the surrounding medium, creating a cloud of hot plasma called H II region. This plasma contains ionised Hydrogen and free electrons at about 10^4K (Rouan [2011]).

The formation happens when a massive star begins to emit ionising photons. As these photons travel outwards, the neutral hydrogen atoms in the surrounding interstellar medium is ionised. An ionisation front propagates outwards until a balance is reached between the rate of ionization and the rate of recombination of electrons and protons. This equilibrium defines the Strömgren radius, R_S, within which virtually all hydrogen is ionised.

As hydrogen is available, new stars can form inside H II regions. However, the ionising radiations of the central massive star will threaten this process of star formation. H II regions are good tools in understanding a galaxy, as these regions are used to obtain a large-scale picture of the star-formation processes in galaxies (Kennicutt and Hodge [1980]) or to constrain galactic chemical evolution theories(Carigi et al. [2019]).

CHAPTER 3

X-ray Astronomy

3.1 The Genesis and Evolution

The discipline of X-ray astronomy represents a relatively nascent field within the astrophysical sciences, emerging less than a century ago. Its inception was contingent upon the technological advancements that enabled the transcendence of Earth's atmospheric barrier for astronomical observations. The inherent opacity of the terrestrial atmosphere to X-ray radiation, stemming from its absorption and interaction with atmospheric constituents, necessitated extraterrestrial platforms for detection. Before the advent of balloon-borne, rocket-based, and ultimately space-based methodologies, astronomical inquiry was confined to the optical, near-infrared, and radio portions of the electromagnetic spectrum, wavelengths that exhibit minimal atmospheric attenuation. The advent of space-based astronomy inaugurated access to previously inaccessible spectral regimes, including X-rays, gamma rays, ultraviolet, and infrared emissions, thereby significantly expanding the observable electromagnetic landscape.

The first successful detection of extraterrestrial X-ray emission was achieved in 1949 by Friedman (Friedman et al. [1951]), who deployed an X-ray detector on a rocket to attain sufficient altitude for the first X-ray imaging of the Sun. Given the solar X-ray luminosity as a benchmark, it was initially posited that stellar X-ray emission would be too feeble for detection from more distant celestial objects, leading to the prevailing notion of a sparsely populated X-ray sky. This paradigm shifted decisively thirteen years later with a rocket experiment conducted by (Giacconi et al. [1962]), an event widely recognized as the genesis of modern X-ray astronomy. While the primary objective of this mission was the investigation of lunar X-ray emission, the data unexpectedly revealed an X-ray source of considerably greater intensity than anticipated. This serendipitous discovery was subsequently identified as Scorpius X-1 (Giacconi et al. [1964]), a low-mass X-ray binary and the brightest extrasolar X-ray source in the sky. Giacconi's seminal contributions to the initiation and development of X-ray astronomy were acknowledged with the Nobel Prize in Physics in 2002. The detection of unforeseen extrasolar X-ray sources catalyzed the field, driven by the imperative to identify novel emitters, characterize their X-ray properties, and elucidate the physical processes responsible for the generation of such high-energy radiation.

Following this foundational discovery, a series of balloon-borne experiments were conducted, offering the advantage of extended observation durations, spanning hours or even days, in contrast to the brief data acquisition windows afforded by rocket flights. A pivotal advancement occurred in 1970 with the launch of UHURU (Jagoda et al. [1972]), the first dedicated X-ray astronomy satellite. Within its initial operational day, UHURU amassed a greater volume of X-ray data than all preceding rocket and balloon missions combined (Arnaud et al. [2011]) and executed the first all-sky survey in the 2–20 keV energy band. The launch of the Einstein Observatory (Giacconi [1980]) in 1978 marked another significant milestone, as it was the first satellite equipped with X-ray focusing optics, enabling unprecedented sensitivity in observations. Subsequently, in 1990, the German ROSAT (Roentgen Satellit) mission (Trümper [1982]) was launched, which detected over $150,000$ sources during its all-sky survey in the 0.1–2.5 keV energy range. These pioneering missions laid the groundwork for the sophisticated X-ray observatories that continue to shape our understanding of the high-energy universe.

Contemporary advancements in X-ray astronomy continue to push the boundaries of our understanding of the high-energy universe. Building upon the legacy of missions like XMM-Newton and Chandra, significant progress has been achieved in enhancing the capabilities of X-ray telescopes. These advancements encompass improved spectral resolution, enabling finer distinctions in the energy of detected X-rays; superior spatial resolution, allowing for more detailed imaging of cosmic sources; and enhanced timing resolution, crucial for studying dynamic phenomena such as pulsations and flares. Furthermore, the overall sensitivity of X-ray telescopes has been significantly increased, allowing for the detection of fainter and more distant objects.

A notable recent development is the successful launch of the X-Ray Imaging and Spectroscopy Mission (XRISM) in September 2023. This collaborative mission between JAXA and NASA, with European Space Agency (ESA) participation, is now operational and provides high-resolution X-ray spectroscopy of the most energetic objects and events in the cosmos, probing the evolution of the Universe and the structure of spacetime.

Looking towards the future, several ambitious X-ray observatory projects are underway. The NewATHENA (Advanced Telescope for High-ENergy Astrophysics), a flagship mission of the ESA, is in its development phase, with a planned launch in 2037. NewATHENA will operate in the $0.2 - 12$ keV energy range and promises to offer spectroscopic and imaging capabilities that exceed those of current generation observatories by at least an order of magnitude. Its primary goals include mapping hot gas structures, determining their physical properties, and tracing the evolution of black holes and galaxy clusters.

These ongoing developments and future missions underscore the continued dynamism of X-ray astronomy, promising groundbreaking discoveries and a deeper understanding of the extreme environments and phenomena that shape our Universe. Future chapters will delve into the physical mechanisms responsible for X-ray production and the advanced detector and optics technologies that underpin these cutting-edge observatories.

3.2 X-ray Producing Processes

Various high-energy mechanisms can generate X-rays. These processes can be broadly categorised into thermal processes and non-thermal processes involving thermally distributed particles. This section provides an introduction to some of the key mechanisms relevant to X-ray astrophysics.

3.2.1 Processes Occurring in Thermal Gases

Black-Body Radiation

Black-body radiation can constitute a form of thermal X-ray emission. A black body is an idealized object characterized by zero reflectivity and thermodynamic equilibrium. Consequently, an object that absorbs all incident radiation must also re-emit it. The emitted spectrum of a black body is radiated isotropically in all directions and exhibits a characteristic shape described by Planck's law:

$$B_\nu(T) = \frac{2h\nu^3}{c^2} \frac{1}{\exp(h\nu/k_B T) - 1}$$

where:

- B_ν: spectral radiance in $\mathrm{W\,sr^{-1}\,Hz^{-1}\,m^{-2}}$
- ν: frequency of the emitted radiation
- T: temperature of the black body
- h: Planck constant
- k_B: Boltzmann constant
- c: speed of light in vacuum

The shape of this spectrum is solely dependent on the temperature of the black body, independent of the frequency and incident angle of the absorbed radiation. The temperature of the black body can be determined from the peak of the emitted spectrum via Wien's displacement law, which states that the frequency at maximum intensity, $\nu_{\max}$, is given by $\nu_{\max} = 5.879 \times 10^{10} \times T\,\mathrm{Hz/K}$ (or in terms of wavelength λ, $\lambda_{\max} = \frac{0.002898}{T}\,\mathrm{K\,m}$). Many astrophysical objects, such as stellar photospheres, emit black-body radiation. For the peak of the emitted spectrum to fall within the X-ray regime, a black-body temperature of approximately $10^6 - 10^8\,\mathrm{K}$ is required. Such high temperatures are encountered, for instance, on the surfaces of young neutron stars.

Thermal Bremsstrahlung

Bremsstrahlung, or "braking radiation," is emitted whenever a charged particle is deflected by an electric field. This occurs, for example, when an electron passes sufficiently close to an ion for electromagnetic interaction to take place. This interaction causes the electron to change direction, resulting in the emission of a photon. As the electron radiates, it loses kinetic energy. Thermal bremsstrahlung is produced when the emitting plasma is in thermal equilibrium, meaning all particle species share the same temperature and follow a Maxwell-Boltzmann velocity distribution. The emitted radiation forms a continuum spectrum with an exponential cutoff at higher energies. The intensity I of this emission is given by:

$$I \propto Z^2 n_e n_i \sqrt{k_B T} \exp(-h\nu / k_B T)$$

where:

- Z: atomic number of the ions
- n_e: electron density of the plasma
- n_i: ion density of the plasma
- k_B: Boltzmann constant
- T: temperature of the plasma
- h: Planck constant
- ν: frequency of the generated radiation

Significant amounts of X-rays are produced through thermal bremsstrahlung when the plasma temperature exceeds $\sim 10^6\,\mathrm{K}$. In addition to this continuum emission, such plasmas typically exhibit line emission resulting from fluorescence.

Fluorescence Lines

In plasmas where heavier elements are not fully ionized, typically at temperatures below $\sim 5 \times 10^7\,\mathrm{K}$, a substantial fraction of energy can be radiated away through fluorescence lines. These lines arise from the deexcitation of an electron to a lower energy level within an atom, accompanied by the emission of a photon. If the plasma temperature is above $\sim 2 \times 10^6\,\mathrm{K}$, these transitions can occur in the X-ray regime. X-ray line emission can originate from energy transitions in the inner electron shells of heavy elements. One mechanism for this is the capture of an electron by a highly ionized particle into an upper shell, followed by the subsequent de-excitation of the electron under photon emission. Another process leading to line emission is the collision of a particle with a high-energy electron. This collision can eject an electron from an inner shell of the particle, and an X-ray photon is produced when an electron from an outer shell transitions to fill the inner shell vacancy. The energies of these transition lines are characteristic of each atomic species, and specific temperatures are required for each transition to be significant. Consequently, these lines serve as valuable diagnostics for determining the chemical composition and temperature of a plasma in thermal equilibrium.

3.2.2 Non-Thermal Processes

Synchrotron Radiation

When a charged particle, moving at relativistic speeds with a velocity component perpendicular to magnetic field lines, traverses a magnetic field, it emits synchrotron radiation. This radiation arises from the Lorentz force, which compels the charged particle to spiral around the magnetic field lines. The continuous change in the particle's direction of motion results in the emission of electromagnetic radiation. The resulting spectrum from an ensemble of charged particles in a magnetic field is determined by the energy distribution of the particles and the strength of the magnetic field. If the underlying population of charged particles, typically electrons, follows a power-law energy distribution, the emitted synchrotron spectrum will also exhibit a power-law form with a peak intensity at a frequency ν given by:

$$\nu = \frac{2\pi eB}{m_e c}\left(\frac{E}{m_e c^2}\right)^2$$

where:

- e: elementary charge of an electron
- B: magnetic field strength
- m_e: mass of an electron
- c: speed of light
- E: energy of the electron

The generation of X-ray synchrotron radiation necessitates a relativistic population of electrons and a strong magnetic field, typically on the order of $\sim 10^6$ G.

Comptonization

Another significant non-thermal process in various astrophysical environments is comptonization, which is a consequence of the inverse Compton effect. The Compton effect itself describes the scattering of a photon by a charged particle, predominantly electrons, wherein the photon loses energy and the charged particle gains energy due to the recoil. This occurs when the energy of the photon ($E = h\nu$) exceeds the energy of the charged particle ($E = \gamma mc^2$, with $\gamma = 1/\sqrt{1 - v^2/c^2}$ being the Lorentz factor). The energy loss of the photon manifests as an increase in its wavelength λ, described by:

$$\Delta\lambda = \lambda_f - \lambda_i = \frac{h}{mc}(1 - \cos\phi)$$

where:

- $\Delta\lambda$: change in wavelength of the photon
- λ_f: wavelength of the photon after scattering

- λ_i: wavelength of the photon before scattering
- h: Planck constant
- m: mass of the particle
- c: speed of light
- ϕ: scattering angle of the photon

Notably, the change in wavelength depends on the scattering angle, but not on the initial energy of the photon.

Conversely, if the particle energy is greater than the photon energy, the inverse process occurs: the photon gains energy (is up-scattered), and the particle loses energy. This inverse Compton effect is prevalent in astrophysical hot plasmas or populations of energetic electrons, such as in the coronae of black holes. When inverse Compton scattering occurs repeatedly and the scattered photons can subsequently escape the population of hot particles, it can lead to effective cooling of the plasma. This process, termed comptonization, results in a characteristic spectral shape for the observed emission from the hot particle population, typically exhibiting a power-law with a high-energy exponential cutoff.

The physical processes outlined in this section are fundamental to understanding the origin of X-ray emission from a multitude of cosmic sources. The subsequent section will discuss various methods employed to detect this high-energy radiation.

3.3 Detection of X-ray Emission

This section discusses the various techniques and technologies employed for the detection of X-rays. The first part focuses on different non-focusing and focusing imaging techniques, while the second part details X-ray detectors, with a particular emphasis on modern, imaging semiconductor detectors.

3.3.1 Imaging Techniques

Imaging X-rays presents a significant challenge due to their absorption by conventional glass lenses and the requirement for very shallow incident angles for reflection from mirror surfaces (Staubert [2008]). The following subsections discuss different non-focusing and focusing techniques utilized in X-ray imaging systems.

Non-Focusing Optics

The earliest optical systems employed for X-ray imaging were non-focusing optics, primarily utilizing collimators. These devices consist of tubes fabricated from X-ray opaque materials, positioned in front of the detector to restrict its field of view (FOV) to a specific region of the sky. The first x-ray source outside the solar system was recorded by a rocket with three Geiger counters, where seven individual mica windows were attached to the entrance apertures of each of these three counters (Giacconi et al.

[1962]). Collimators were also implemented on the UHURU satellite. To address the substantial physical dimensions of traditional collimators, honeycomb collimators were developed. These comprise a dense array of small collimator tubes arranged in a honeycomb pattern. This design significantly reduces the overall size of the collimator, albeit at the cost of a diminished effective detector area due to the opaque walls of the honeycomb structure partially obstructing incident radiation.

As these non-focusing optics provide no inherent spatial information about the source's location within the FOV, single-pixel detectors can be used without any loss of positional data. However, even without spatially resolving detectors, information regarding the number of sources within the FOV and their celestial coordinates can be acquired through the use of rotation modulation collimators (RMCs). These devices consist of two grids of X-ray absorbing material placed in front of the detector, with one grid undergoing rotation relative to the other. The resulting temporal variation in the detected X-ray flux, known as a light curve, exhibits a specific frequency and modulation pattern that is dependent on the source's position within the FOV. The frequency of this signal enables the determination of the projected source image's distance from the rotational axis of the collimator, while the phase of the modulation curve yields information about the position angle of the projected source image. This technique marked a considerable improvement in the imaging of cosmic X-ray sources, allowing for the discrimination of multiple point sources within a shared FOV. This type of optics was utilised, for example, on the High Energy X-ray Experiment (HEXE) onboard the MIR space station (Reppin et al. [1985]).

While non-focusing optics were instrumental in early X-ray astronomy, their limited angular resolution and sensitivity prompted the development of focusing optics. Grazing incidence mirrors, such as Wolter telescopes, revolutionized X-ray imaging by concentrating photons onto a small detector area, significantly improving sensitivity and resolution (Wolter [1952]).

Focusing Optics

The advent of focusing optics represented a transformative development in X-ray astronomy, enabling substantially enhanced sensitivity and spatial resolution. Owing to the high energy of X-ray photons, conventional refractive optics are impractical. Instead, X-ray telescopes leverage the principle of grazing incidence reflection.

Wolter Telescopes: The most successful and widely adopted design for focusing X-rays is the Wolter telescope. This configuration employs a series of nested, coaxial, and confocal mirrors. The primary designs include: the Wolter Type I, consisting of a paraboloid followed by a hyperboloid (Fig 3.1); the Wolter Type II, also a paraboloid and hyperboloid but with a virtual focal point between them; and the Wolter Type III, employing a paraboloid and an ellipsoid. Incident X-rays strike the surface of the first mirror at a very shallow angle and are reflected to graze the surface of the second mirror, ultimately converging to a focal point. The nesting

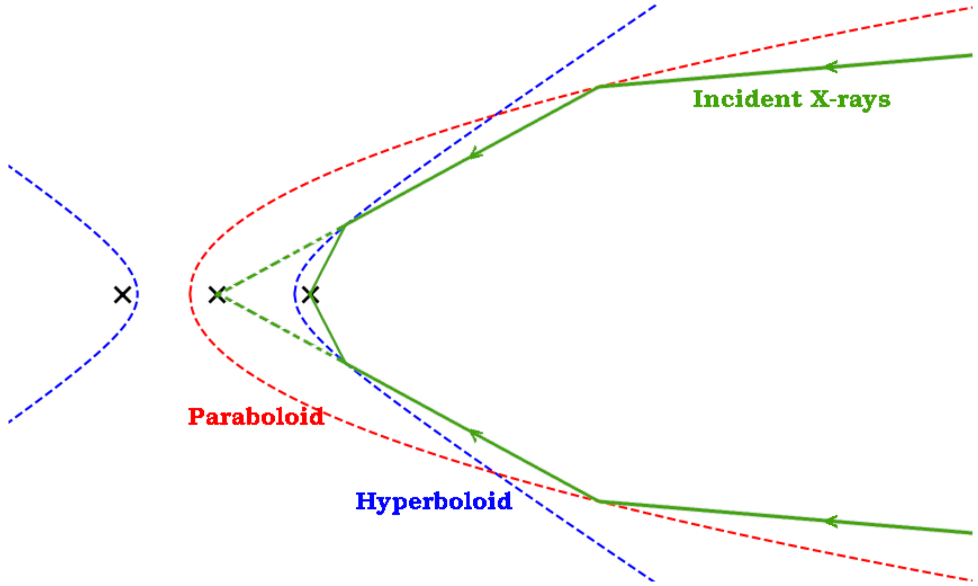

Figure 3.1: Schematic illustration of the arrangement of mirrors in a Wolter type I telescope.

of multiple mirror shells concentrically increases the effective collecting area of the telescope.

The extremely shallow grazing angles (typically less than a few degrees) are necessitated by the fact that the refractive index of most materials for X-rays is slightly less than unity. According to Snell's law, this condition leads to total external reflection when the incident angle is sufficiently small. The critical angle for total external reflection is energy-dependent, decreasing with increasing X-ray energy. This energy dependence imposes a limitation on the effective energy range of grazing-incidence telescopes.

Contemporary X-ray observatories such as Chandra (Weisskopf et al. [2002]) and XMM-Newton (Jansen et al. [2001]) utilize Wolter Type I optics with multiple nested mirror shells, achieving arcsecond-level angular resolution and high sensitivity. The precise fabrication and alignment of these intricate mirror systems are paramount for obtaining high-fidelity X-ray images.

Alternative Focusing Techniques: While Wolter telescopes constitute the dominant technology, alternative focusing techniques have been explored or are currently under development for specific energy ranges or specialized applications. These include:

- Kirkpatrick-Baez (KB) Microscopes: Employing two orthogonal, concave cylindrical mirrors to achieve X-ray focusing. Primarily utilized in laboratory settings and for specialized imaging tasks.

- Multilayer Coatings: The application of thin layers of different materials to mirror surfaces can enhance reflectivity at higher X-ray energies and larger grazing angles through the phenomenon of constructive interference. This technology is incorporated into some hard X-ray telescopes.

- Diffractive Optics (e.g., Fresnel Zone Plates): These optical elements utilize diffraction to focus X-rays. While presenting fabrication challenges for high efficiency in astronomical applications, they hold potential for future lightweight X-ray telescope designs.

The development and implementation of focusing X-ray optics represent a crucial milestone in the field, enabling detailed imaging of cosmic X-ray sources and facilitating significant advancements in our understanding of high-energy astrophysical phenomena.

Another method for identifying individual sources and determining their position within the FOV involves the use of coded masks. This imaging technique necessitates spatially resolving detectors. The coded masks are placed in front of the detectors and consist of intricate patterns of an X-ray absorbing material (e.g., tungsten) interspersed with X-ray-transmissive apertures. The pattern is specifically designed such that the shape of the shadow cast upon the detector by an X-ray source is unique to the source's position within the FOV. Consequently, the source's location can be reconstructed by deconvolving the recorded shadow pattern. This technique remains valuable today for imaging hard X-rays ($\gtrsim 20$ keV), which are only efficiently reflected at very small incidence angles, thus requiring large focal lengths that are challenging to implement in satellite missions.

A significant enhancement in the sensitivity and resolution of X-ray imaging systems was achieved with the launch of the first X-ray focusing optics on the Einstein Observatory satellite in 1978 (Giacconi [1980]). Focusing X-rays using mirrors presents a non-trivial challenge due to the small incident angles required for their reflection. This critical angle for reflection increases with the atomic number and density of the reflecting material and with the wavelength of the incident radiation. To maximize this angle, the reflective surfaces of X-ray mirrors are often coated with elements such as gold or iridium, which possess a high atomic number and density.

For photons with energies of 1 keV, the critical angle for reflection is only approximately $1°$. Such small reflection angles would necessitate very long focal lengths. To mitigate this, a specialized mirror configuration known as a Wolter-I mirror is employed in X-ray astronomy (Wolter [1952]). In this configuration, the X-rays undergo two reflections: first from a paraboloidal mirror shell and then from a hyperboloidal mirror shell. This double reflection allows for a considerable reduction in the focal length, for example, to approximately 7 metres for photons with an energy of around 15 keV. To compensate for the limited effective area of each individual mirror shell, which arises from the small reflection angle for X-rays, multiple mirror shells with varying radii are nested coaxially and confocally within each other.

Wolter-I mirror telescopes are commonly utilized in modern X-ray astronomy, as exemplified by the X-ray telescopes of XMM-Newton, each comprising 58 nested mirror shells with a minimum separation of 1 mm between individual shells. Typically, such focusing optics are used in conjunction with a spatially resolving X-ray detector to enable accurate image reconstruction. Some of these detectors are introduced in the following section.

3.3.2 X-ray Detectors

Since the discovery of X-rays in 1895 (Röntgen [1895]), X-ray detectors have undergone rapid development. The devices employed have evolved significantly, with continuous improvements in performance. This section provides a concise overview of the different types of detectors used in X-ray astronomy, with a particular focus on modern semiconductor detectors.

The Beginning

The discovery of X-rays (Röntgen [1895]) were on conventional optical film plates, which are also sensitive to X-ray photons. Later, in 1908, proportional counters were developed, which were essentially capacitors filled with a noble gas (Rutherford and Geiger [1908]; Pfeffermann [2008]). When X-rays enter the proportional counter, electron-ion pairs are generated via the photoelectric effect. An applied voltage across the capacitor separates these electron-ion pairs and accelerates primarily the electrons, which subsequently collide with other atoms. This process leads to the creation of further free electrons, which are attracted by the anode and can be measured as a current. With appropriate voltage settings, the number of electrons generated is proportional to the energy of the incident photon.

For the detection of hard X-rays with energies exceeding 15 keV, inorganic scintillation counters can be utilized (Kendziorra [2008]). These detectors consist of a scintillator crystal coupled to a photomultiplier tube. When an incident X-ray photon strikes the scintillator, it can be absorbed through the photoelectric effect, and the resulting photoelectron can excite multiple atoms within the crystal. As these excited atoms subsequently undergo radiative de-excitation, they emit photons in the optical wavelength range. These optical photons then interact with the photomultiplier, generating free electrons via the photoelectric effect at the photocathode. These photoelectrons are subsequently accelerated and amplified through a series of dynodes within the photomultiplier by applied electric fields. The resulting output current allows for the measurement of both the intensity and the energy of the incoming X-ray radiation.

Currently, semiconductor detectors are the most prevalent type of detectors used in astronomy for X-ray detection. These will be discussed in detail in the following subsection.

Semiconductor Detectors

In contemporary X-ray astronomy, semiconductor detectors are the most commonly employed type of detector. In these devices, photon detection is based on the internal photoelectric effect within a doped semiconductor material (e.g., silicon). Incident photons with energies greater than or comparable to the material's band gap can create electron-hole pairs within the semiconductor lattice. To prevent immediate recombination of these charge carriers, an applied voltage is used to separate the electron-hole pairs and store the electrons in a potential well present in each pixel. This fundamental concept is implemented in various types of semiconductor detectors, with the primary differences lying in the readout mechanisms.

A widely used type of semiconductor detector is the charge-coupled device (CCD), which is read out by sequentially shifting the photon-induced charges through the device until a readout node is reached. In a CCD, each pixel typically comprises three electrodes onto which different voltages can be applied. During the detector's exposure time, the photoelectrons generated within each pixel are accumulated under the central electrode. Following the integration period, the voltages applied to the electrodes are manipulated to cause the collected electrons to shift from pixel to pixel along a pixel row until they reach a readout node. Once each pixel in a row has been read out sequentially using this method, the readout cycle for that row is complete, and a new integration period can commence. The time required for a complete readout cycle depends on the number of pixels per row and represents a trade-off between energy resolution and timing resolution. This readout method offers the advantage of enabling a large number of pixels to be read out by a single readout node and associated electronics.

Another class of semiconductor detectors is the active pixel sensor (APS). In these devices, each pixel is read out individually, for example, by measuring the locally amplified voltage generated by the electrons accumulated within a pixel without the need for charge shifting. Since the readout process does not destroy the collected charge, a signal can be read out multiple times to improve the energy resolution. Subsequently, the pixel is actively cleared of these electrons. A pixel configured in this manner is often located within the center of a macropixel. A macropixel consists of a selectable number of drift rings arranged around a central pixel. The drift rings are cathodes held at progressively less negative potentials towards the pixel center. This potential structure guides the electrons collected within a macropixel towards the central pixel, where the readout occurs. The variable number and shape of the drift rings provide significant flexibility in the size and geometry of a macropixel. The primary advantage of active pixel sensors is their high readout speed (approximately $2\ \mu s$ per line), which is a consequence of the direct readout mechanism that eliminates the need for charge shifting. Furthermore, the local amplification of the signal before readout contributes to a better energy resolution.

CHAPTER 4

XMM-Newton

XMM-Newton is an X-ray satellite of the European Space Agency (ESA), launched on December 10, 1999. In this more than a quarter-century of operations, this telescope has observed stars (e.g., Karmakar and Youngblood [2025]), neutron stars (e.g., Pires et al. [2025]), X-ray binaries (e.g., Avakyan et al. [2025]; La Palombara et al. [2025]), supernovae (e.g., Reguitti et al. [2025]), supernovae remnants (e.g., Vink [2001]), and pulsars (e.g., Alford et al. [2025]). Named after Sir Isaac Newton, reflecting his contributions to spectroscopy and gravity, XMM-Newton is a cornerstone of ESA's Horizon 2000 programme, designed to investigate interstellar X-ray sources through high-throughput spectroscopy and simultaneous imaging in X-ray and optical/ultraviolet wavelengths Watson et al. [2001].

XMM-Newton is equipped with three primary scientific instruments: the European Photon Imaging Camera (EPIC), the Reflection Grating Spectrometer (RGS), and the Optical Monitor (OM). The spacecraft, measuring 10 meters in length with a 16-meter solar array span and weighing 3.8 metric tons, comprises four main sections: the Focal Plane Assembly (FPA), the service module, the mirror support platform, and the mirror modules (ESA: XMM-Newton SOC [2013]). The FPA houses the focal-plane instruments, including two RGS readout cameras, one EPIC pn-CCD, two EPIC MOS-CCD detectors, and associated electronics. Each of the three X-ray telescopes contains 58 nested gold-plated nickel mirrors in a Wolter I geometry, optimized for grazing incidence to focus highly energetic X-rays with a focal length of 7.5 meters and an angular resolution of 6 arcseconds (full width at half maximum). Radiators attached to the EPIC and RGS instruments passively cool the CCDs to mitigate radiation-induced noise, with EPIC MOS-CCDs operating at approximately $-120°$C and the pn-CCD at similar low temperatures ([European Space Agency, 2012]).

XMM-Newton operates in a highly elliptical 48-hour orbit around Earth, inclined at 40degrees, with a perigee of $7,000$km and an apogee of $114,000$ km. This orbit, synchronized to be exactly twice Earth's rotational period, ensures optimal contact with ground stations at Kourou and Yatharagala, enabling real-time data transmission to the Mission Operations Centre at ESOC, Darmstadt, Germany. For approximately 40 hours per orbit, the satellite remains outside Earth's radiation belts, allowing extended, uninterrupted observations of celestial X-ray sources. The orbit's eccentricity maximizes observation time, supporting the mission's goal of sensitive imaging and spectroscopy down to a limiting flux of 10^{-16} erg/s/cm^2.

Among XMM-Newton's instruments, the EPIC is the primary imaging spectrometer, consisting of three cameras: two Metal-Oxide-Semiconductor (MOS) CCD detectors and one pn-CCD detector, each positioned at the focus of an X-ray telescope. The EPIC provides moderate spectral resolution in the 0.1 to 15 keV energy range, comparable to the Advanced Satellite for Cosmology and Astrophysics (ASCA), and is highly sensitive to low surface brightness emission, enabling detailed studies of extended sources like supernova remnants and galaxy clusters. The two MOS-CCD cameras share their mirror modules with RGS grating arrays, which divert approximately 40% of incoming X-rays to a secondary focus for high-resolution spectroscopy, while the pn-CCD camera benefits from a fully open telescope for maximum throughput. The EPIC's CCDs are critical to its performance. These silicon-based semiconductor detectors convert X-ray photons into electron-hole pairs via the photoelectric effect. The charge is then read out and digitized to determine the photon's energy and position. The MOS-CCDs offer higher spatial resolution (6 arcseconds), while the pn-CCD provides greater quantum efficiency and faster readout, ideal for bright sources. To counteract ionizing radiation damage, the CCDs are cooled to reduce dark current to lower the MOS-CCD temperature from $-100°$C to $-120°$C, significantly improving data quality. The temperature maintenance is realised using three-stage radiator system combined with heaters. The EPIC's ability to register photon arrival time, energy, and direction supports temporal variability studies, such as those of X-ray binaries and pulsars.

The RGS, mounted on two of the X-ray telescopes, provides high-resolution spectroscopy in the 0.35 to 2.5 keV range. By dispersing X-rays into their constituent wavelengths using grating arrays, the RGS reveals detailed spectral features of elements like oxygen and iron, aiding in the study of physical conditions in sources such as active galactic nuclei and binary systems. The OM, a 30-cm diameter optical/UV telescope, observes the same regions as the X-ray telescopes in ultraviolet and visible wavelengths, offering complementary data. In orbit, its sensitivity is equivalent to a 4-meter ground-based telescope, supporting multi-wavelength studies of X-ray sources.

XMM-Newton's integrated design, combining high-throughput X-ray telescopes, sensitive instruments, and a strategic orbit, has enabled groundbreaking observations of diverse astrophysical phenomena. The EPIC, with its advanced CCD technology, remains central to the mission's success, delivering high-quality imaging and spectroscopy that continue to advance our understanding of the X-ray universe.

CHAPTER 5

Data and Processing

5.1 X-ray

The observation from the X-ray satellite contains different types of data, including unwanted data. The background components in an XMM-Newton observation can be broadly classified into three: electronic background, photon background, and particle background. The field-of-view will also have many point sources, contaminating the emission from our extended source of interest. Therefore, the data need to be processed, filtered and background-subtracted to obtain useful information about the source. The subject SNR was faint and located in the Large Magellanic Cloud (LMC), i.e., ~ 50 kpc away. All the three detectors were operated in MEDIUM Filter and Full Frame mode during this observation. The exposure time was 40.7, 40.7 and 41.4 ks for the MOS1, MOS2 and pn detectors respectively. After discussing the XMM-Newton data and handling, this chapter briefly introduces other data used in this thesis.

5.1.1 Analysis with XMM-ESAS

The XMM-Newton Extended Source Analysis Software (XMM-ESAS) package provides the tools required for the analysis of spectra and images of extended diffuse emission. It functions in producing images capturing all identified background and foreground elements, facilitating the isolation of true cosmic X-ray emissions. The background/foreground components managed by XMM-ESAS encompass the quiescent particle background (QPB), soft proton flares (SPF), and to a certain extent, solar wind charge exchange (SWCX). XMM-ESAS aids spectroscopy by producing the spectrum of the QPB for the observation (Snowden et al. [2011]). In these spectra produced by MOS and *pn* detectors of the telescope, the MOS spectra are more reliable than the *pn* spectrum. There are two reasons for this credibility issue, one being the poor statistics of the pn corner data. Secondly, a previously underestimated sensitivity of pn corner data to SPFs has been identified by the ESAS team. Consequently, the current pn QPB spectra may not be entirely free of residual SPF emission.

The analysis begins with recreating the event files. There are two ways to achieve this: ”the chains” and ”the procs”, done by the tasks `emchain` or `epchain` and `emproc` or `epproc` respectively. Both processes have the same end result, but the path is different. The chains did not work in this analysis and hence the procs were used.

The subsequent task is `emanom` to exclude the anomalous state CCDs in the further processing. The `emanom` task evaluates the $(2.5 - 5.0$ keV$)/(0.4 - 0.8$ keV$)$ corner hardness ratio to identify anomalous chip, states Snowden et al. [2011]. This task reveals that there are no counts in the soft band as the count rate was sufficiently low. Although in this case it would be impossible to determine the anomaly of chips, the data are useable as there are no counts in the soft band.

Next is the task `espfilt` to filter the soft proton (SP) flares, which works by creating two light curves in the$2.5 - 8.5$ keV band, and creates an X-ray count rate histogram from the FOV data. This process does not eliminate all the traces of SP contamination from the data, but rather only removes time intervals exhibiting significant count rate enhancements. This is evident in Figure 5.1 where the absence of accepted data (green) in light curve indicates a probable residual SP contamination that is filtered.

The next action is to identify and remove the point sources, as they are not the subject here, and thus abate the noise in the data. For this the ESAS package offers the `cheese` task which integrates both MOS and *pn* data for source detection, generating images and exposure maps in a selected single band or in selected soft, hard, and total (combined) bands. It produces source lists that can subsequently be used to create source-excluded spectra and to generate masks for image processing. However, the automatic cheese always counted the subject source as a point source and hence the cheese filter was employed manually. The manual way of identifying point sources is using the task `stinky cheese` where all the regions are marked at first and then the regions of interest are manually deleted from the list of sources, thus producing a region file with only point sources. A mask is then generated with this region file using the task `makemask`, and the SNR is not masked, but the point-sources.

Once the point sources are removed, the QPB spectra is created, which is a two-step process that requires `mosspectra` and `mosback` for mos detectors or `pnspectra` and `pnback` for the pn detector. While the `mosspectra` and `pnspectra` extract QPB spectral information from the corner spectra from each chip of the observation being analyzed, the corner spectra from each chip of the FWC data, and the FOV spectra from each chip of the FWC data, the `mosback` and `pnback` combine this information to create two final products: the QPB spectrum for a specific region within the observed field-of-view and an image of the QPB component in a chosen band. The `mosback` and `pnback` does an augmentation of the corner spectra from a database of corner data extracted from the public archive, because of the relatively low count rate in the corner data. Figure 5.1 shows the temporal filtering results for the detector `mos1`.

5.1.2 Facilitating Image Production

To facilitate the generation of images, it is imperative to ascertain: 1) the magnitude and spectral characteristics of the residual SP emission, and 2) the intensity of the solar wind charge exchange (SWCX) emission. Binning was done by using the Ftool `grppha` and the data was grouped with a minimum of 100 counts per channel for the first spectral fit. For the spectral fitting process of multiple regions which are linked, the task

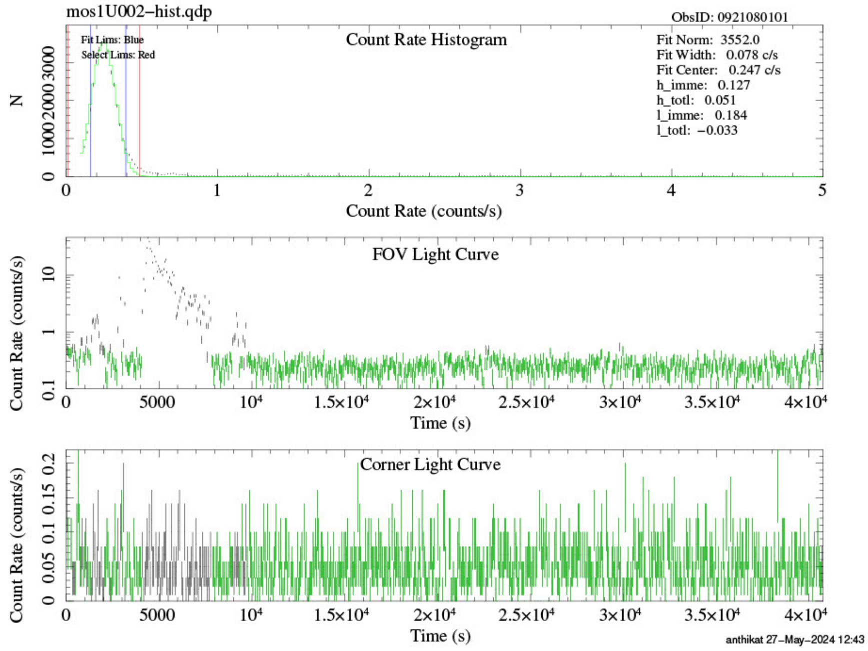

Figure 5.1: Temporal filtering results for the MOS1 detector. The upper panel plots the light curve histogram derived from the smoothed light curve for the $2.5-8.5$ keV band from the field-of-view (FOV) and the blue vertical lines show the range for the Gaussian fit, the green curve shows the Gaussian fit, while the red vertical lines show the upper and lower bounds for filtering the data, the middle panel displays the $2.5-8.5$ keV band FOV light curve, and the lower panel displays $2.5-8.5$ keV band light curve from the unexposed corners of the instrument. In the bottom two panels green points indicate accepted data while black points indicate data excluded by the filtering algorithm.

`proton scale` from version 20.0 of XMM-SAS was used to average total soft proton intensity from the detector map for a specified region. The older version was called for this task as the 21.0 version's `protonscale` was found faulty for my case.

With the areas determined by the `proton_scale`, an XSPEC model was used to fit full-field (excluding point sources) spectra. The cosmic X-ray background, the instrumental lines, the solar wind charge exchange and the residual soft proton flares are fit to the data. With the fitted values of the SP component from XSPEC, the task `proton` is used to produce images in detector coordinates of the model residual SP contamination.

5.1.3 Modelling and Fitting with XSPEC

The reduced spectra were modelled and fit using XSPEC (Arnaud [1996]). XSPEC is a general X-ray spectral-fitting program with a wide range of theoretical models and the options to easily add these models together. The different models used for the fits were vnei (variable non-equilibirum ionisation) model for the ejecta, apec (Astrophysical Plasma Emission Code) model for the background, and TBabs and TBvarabs for the absorption by the intervening ISM.

In our observation, the x-ray ejecta undesirably entered a chip gap in the *pn* detector. Consequently, in addition to the spectral analysis performed on the combined *mos1*, *mos2* and *pn*, a separate spectral analysis was performed using a data combination that excluded the *pn* detector (Fig 5.2).

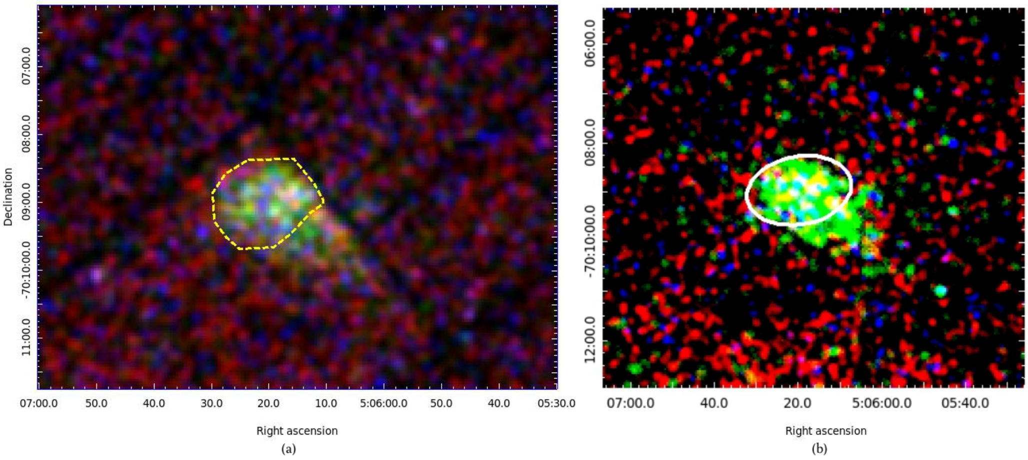

(a)

(b)

Figure 5.2: The regions used for spectral analysis, indicated on the three-color *XMM-Newton* images where the red layer is the X-rays in the range 300 eV - 700 eV, green 700 eV - 1100 eV and blue 1100 eV to 1500 eV. The combined images are shown for (a) MOS1, MOS2, and pn detectors, and (b) MOS1 and MOS2 detectors only.

For the spectral fitting of the ejecta, a background fit was also required, and these regions are marked in Fig 5.3, where region marked as 1 is the background region used for the first fit and the region marked as 2 is the region used for the latter fit. The following chapter will explain the first (Fig 6.5) and latter (Fig 6.6) fits in detail.

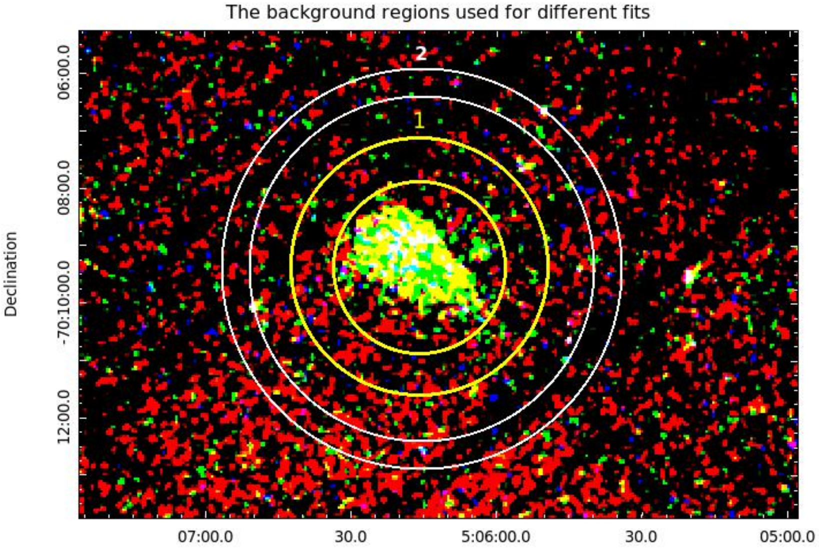
The background regions used for different fits

Figure 5.3: The regions from which the background was fit for the x-ray spectra, marked in the three-color image of XMM-Newton.

5.1.4 eROSITA

Other than the dedicated observation from XMM-Newton, the data from extended Roentgen Survey with an Imaging Telescope Array (eROSITA) (Predehl et al. [2021]; Sunyaev et al. [2021]) was also helpful, particularly in the primary detection by Zangrandi et al. [2024]. This X-ray telescope conducts all-sky survey in the medium X-ray energy band (0.2–10 keV). Zangrandi et al. [2024] applied a Gaussian gradient magnitude (GGM) filter, which calculates the magnitude of the gradient of an image using Gaussian derivatives, on the eRASS:4 images.

5.2 Optical

The optical data in this thesis is from Magellanic Cloud Emission Line Survey (MCELS) (Smith and MCELS Team [1999]) supplemented by the narrow-band filters H α ($\lambda_c = 6563\AA$, FWHM = 30 Å), [S II] ($\lambda_c = 6724\AA$, FWHM = 50 Å) and [O III] ($\lambda_c = 5007\AA$, FWHM = 50 Å). I used continuum-subtracted images around the emission lines. These images were taken at the University of Michigan (UM) Curtis Schmidt telescope at Cerro Tololo Inter-American Observatory (CTIO).

5.3 Radio

The radio continuum data from the Australian Square Kilometre Array Pathfinder (ASKAP), in particular, the publicly available four-pointing mosaic of the LMC is also used in the thesis. The radio-continuum image covers 120 deg^2 at 888 MHz. The sensitivity of the map at 888 MHz is 58 μJy beam^{-1} (Filipović et al. [2022]).

The Magellanic Mopra Assessment (MAGMA) (Wong et al. [2011]; Wong et al. [2017]) data is used to locate the molecular clouds in the LMC. MAGMA is a CO mapping survey of the Large and Small Magellanic Clouds using the 22-m Mopra Telescope of the Australia Telescope National Facility. For the LMC, the angular resolution was 11 pc in the CO(1–0) line. This can resolve only the large giant molecular clouds.

CHAPTER 6

The Supernova Remnant J0506-7009

This section presents a detailed analysis of the subject SNR of this study. The thesis will first introduce its host galaxy, the Large Magellanic Cloud (LMC), providing a context for its formation and evolution, and then present the spectral analysis and discuss the SNR. Subsequently, the thesis will delve into the immediate environment surrounding the SNR, examining the characteristics of the interstellar medium in its vicinity, including its presence within a superbubble and its proximity to massive stars. This analysis is crucial for understanding the physical processes that shape the remnant and interpreting the observational data.

6.1 The Large Magellanic Cloud

The Large Magellanic Cloud hosts our subject SNR. The LMC is a satellite galaxy of Milky Way galaxy, at a distance of ~ 50 kpc from our solar system (Pietrzyński et al. [2019]). Compared to our Galaxy, the gas-to-dust ratio is ~ 4 times higher(Koornneef [1982]) and the metal abundance $\sim 3-4$ times lower(Rolleston et al. [2002]). Zangrandi et al. [2024] reports a total of 77 confirmed SNRs in the LMC along with 47 candidates.

6.2 The Supernova Remnant

The SNR J0506-7009 is located at $\mathrm{RA} = 05^{\mathrm{h}}\,06^{\mathrm{m}}, \mathrm{Dec} = -70^{\circ}\,09'$ (J2000.0). The eROSITA observation of the area including the subject SNR is shown in figure 6.1 and the SNR as observed by MCELS is presented in Figure 6.2. The contours marked in the MCELS data are $\mathrm{S\,II}/\mathrm{H}\,\alpha > 0.67$. This indicates a shocked nebula (Fesen et al. [1985]). Furthermore, we see radio emission (Figure 6.3) corresponding to the elliptical forward shock in the optical emission, which also indicates a SNR. After the blast wave passes through a cloud as it expands to the ambient medium, the shocked interstellar material cools down. This cooling can be seen as optical emission in older remnants (Fesen et al. [1985]). Figure 6.4 shows the remnant as seen in eROSITA, MCELS and ASKAP with contours marking dominant X-ray emission, shock or non-thermal emission. The figure is taken from Zangrandi et al. [2024]. Here, for the second image, Gaussian gradient magnitude (GGM) filter is applied to the eROSITA count rates. Therefore, the X-ray spectrum was fit with the source modeled as an SNR. It should be noted here that the estimation of the forward shock from the optical was by eye. We not only see the elliptical shell, but also a circular shell, which is marked in Figure 6.2. This circular shell is assumed to be the forward shell of the remnant in the calculations later-on. Makarenko et al. [2023] explains how [S II] lines traces the thin shell of the forward shock.

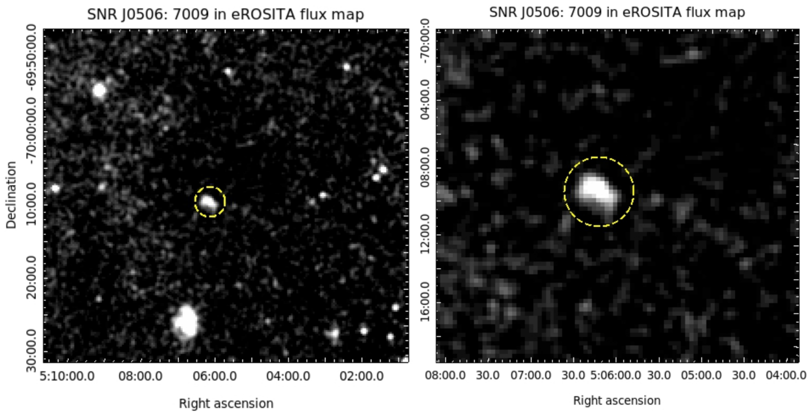

Figure 6.1: SNR J0506-7009 as seen by eROSITA

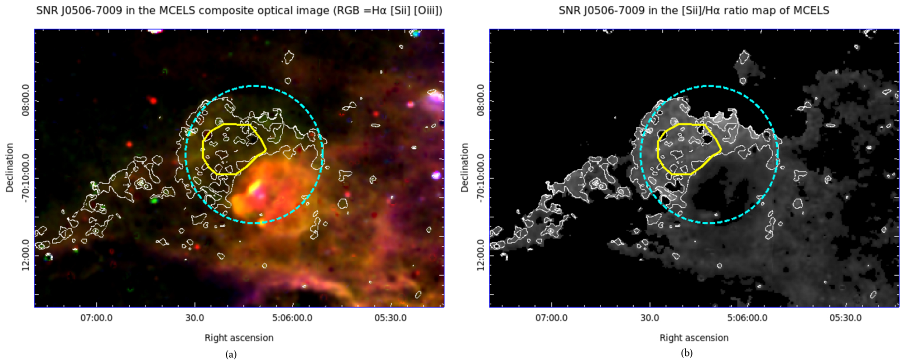

Figure 6.2: The SNR in MCELS data. (a) The three-color image from the MCELS data is a superposition of Hα emission in red, [S II] in green and [O III] in blue. The X-ray emitting region used for the spectral analysis is marked in yellow and the visually fitted optical extent of the SNR in cyan. The contours marked in the MCELS data (b) are [S II] / Hα ratio > 0.67.

Figure 6.3 shows the region of X-ray emission used for the first spectral analysis and the figure 6.5 is the best fit for this emission. The fit results are tabulated in 6.1.

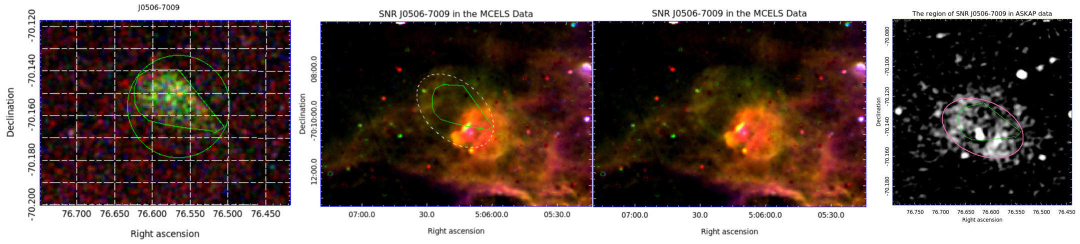

Figure 6.3: The region of the SNR used for the first X-ray analysis.

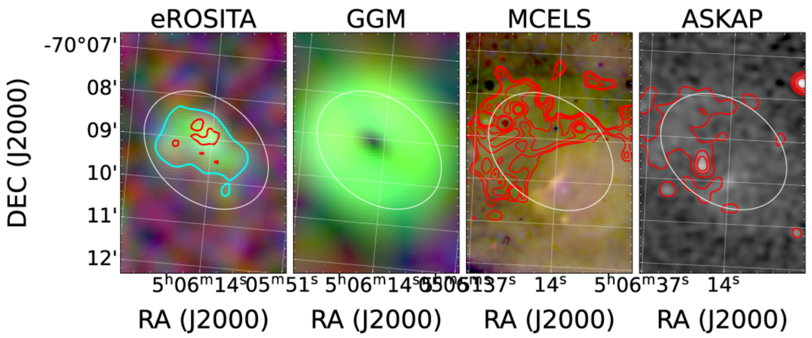

Figure 6.4: The eROSITA count rate three-colour image with red: 0.2–0.7keV, green: 0.7–1.1 keV, and blue: 1.1–5.0keV; the GGM filter image applied to the eROSITA count rate; the MCELS three-colour image with red: H α, green: [S II], and blue: [O III]; and the ASKAP radio continuum image in the upper panel, in order from left. The white ellipses shows the area of higher X-ray emission from whoch the count rates were determined. The cyan (red) contours in the eROSITA three-colour image show the detection at 1 σ (3σ) over the background in the energy band 0.2–1.1 keV. The contours in the optical image represent [S II]/H$\alpha > 0.67$. The contours in the radio image show the non-thermal emission calculated. Figure from Zangrandi et al. [2024]

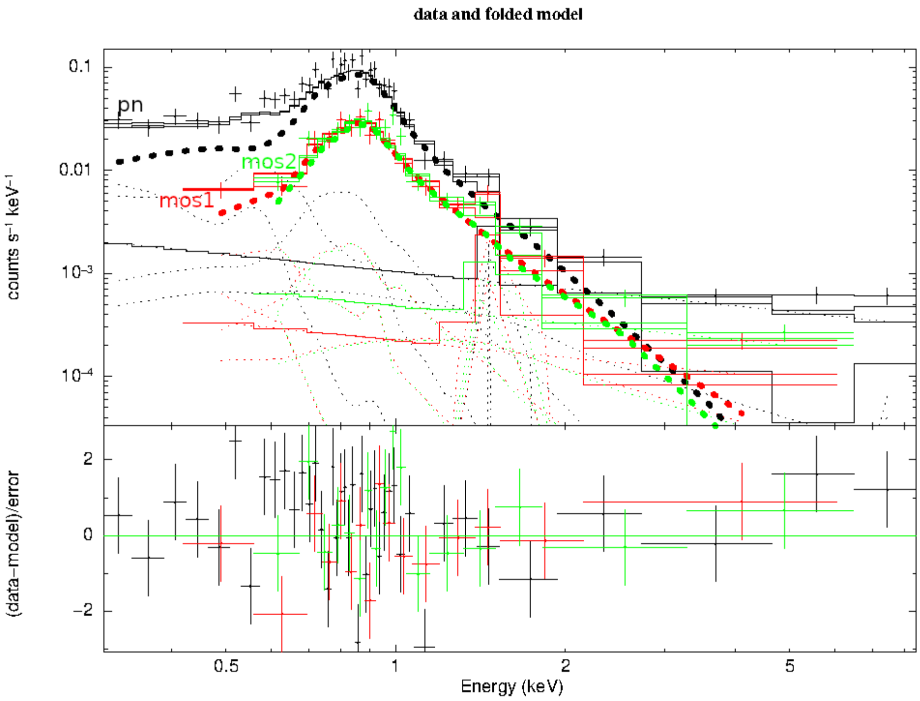

Figure 6.5: The spectra with fit for the elongated X-ray emission. Upper panel: the spectra from the detectors pn (black), mos1 (red) and mos2 (green) with models. The thick dotted lines are the vnei models. Lower panel: the delta chi-square of the fit.

However, we see that this X-ray emission extends into a circular structure in the MCELS (6.5). Therefore, separate fits were done for this region split into two, based on this structure seen in the optical wavelengths (7.2). The processed spectra were fit using c statistics (Fig. 6.6) and the fit results are tabulated in table 6.2. First the region a was fitted and then the same model was used to fit b, allowing only the absorbing foreground Hydrogen density(N_H) to be free. Hence, only the fit results of region a are shown here. Three fits were made – a: freezing neither Oxygen nor Iron abundances, b: freezing Oxygen abundance to the observed LMC

Parameter	Value
H column density (units)	$< 0.022 \cdot 10^{22}$
Temperature kT (keV)	$0.76^{+0.03}_{-0.02}$
Iron abundance ($X/X_{\odot}$)	$0.78^{+0.05}_{-0.16}$
Ionization timescale τ ($10^{11} s/cm^3$)	$> 1.35 \cdot 10^{11}$
Normalization K ($10^{-6}/cm^5$)	$4.74^{+0.82}_{-0.74} \cdot 10^{-05}$

Table 6.1: The first fit data.

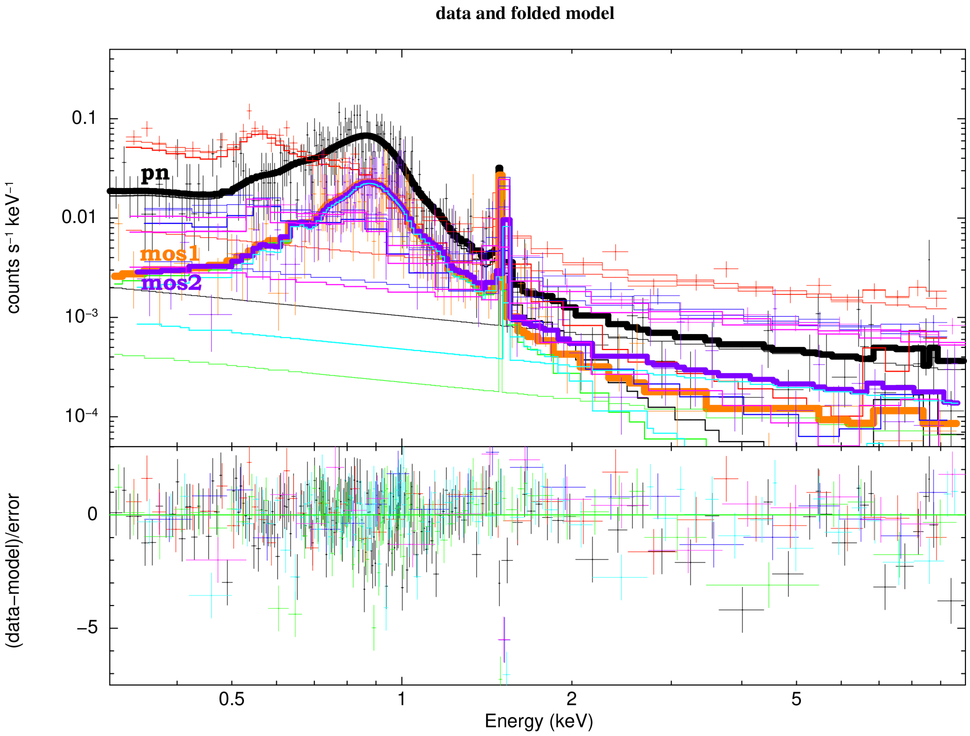

Figure 6.6: The spectra and the fit for the region a.

ISM average of 0.21 Z$_{\odot}$ (Maggi, P. et al. [2016]) and c: freezing Oxygen abundance to the generalized LMC average 0.5 Z$_{\odot}$ (Russell and Dopita [1992]). The values of absorbing Hydrogen column density N_H could not be well constrained for the region a and hence was frozen to 0.00 cm^{-2}. The absorbing Hydrogen column density N_H of the region b is $0.88^{+0.10}_{-0.09}$ $\times 10^{22}$ cm^{-2}. This suggests the presence of a Hydrogen dense nebula in the foreground of the remnant, and the X-ray emission of region b is either part of the region a and is absorbed by the cloud, or is a different source.

The abundance ratio of Oxygen to Iron is signficant in typing the remnant. The [O]/[Fe] abundance ratios are listed in table 6.3. The ratio for the LMC, $[O]/[Fe]_{LMC}$, is 0.60 (Maggi, P. et al. [2016]). As CC-SNe produce large amounts of light elements, such as O, Ne, Mg, or Si, compared to a small amount of Fe, and Type Ia SNe predominantly produce Fe, $\frac{[O]/[Fe]}{[O]/[Fe]_{LMC}} \ll 1$ indicates a Type Ia progenitor (Maggi, P. et al. [2016]). According to (Bozzetto et al. [2014]), the O/Fe ratio is expected to be 0.3–0.7

Parameter (Unit)	$fit(a)$	$fit(b)$	$fit(c)$
Temperature kT (keV)	$0.76^{+0.04}_{-0.03}$	$0.76^{+0.05}_{-0.04}$	$0.76^{+0.05}_{-0.03}$
Oxygen abundance ($X/X_\odot$)	$0.75^{+3.45}_{-0.54}$	0.21^{frozen}	0.5^{frozen}
Iron abundance ($X/X_\odot$)	< 5.82	$1.19^{+0.49}_{-0.33}$	$1.24^{+0.58}_{-0.33}$
Ionization timescale τ ($10^{11}s/cm^3$)	> 1.45	> 1.2	> 1.435
Normalization K ($10^{-6}/cm^5$)	13.2	$15.4^{+4.4}_{-6.6}$	$14.97^{+6.5}_{-4.4}$
Fit Statistic (dof)	$2082.84(6007)$	$2056.99(6006)$	$2054.66(6006)$

Table 6.2: Spectral fit results. Uncertainties are estimates of upper and lower 90 % confidence ranges. The limits couldn't be constrained for some parameters.

for Type Ia events. Here, the oxygen abundance could not be well constrained, but the estimated abundances indicate that the SNR studied here is likely to be from a Type Ia SN explosion. To provide a better feeling on what abundance ratio to expect in either case, I derived this ratio for LMC SNRs having a well secured type (Table 6.2).

	[O]/[Fe]	$\frac{[O]/[Fe]}{[O]/[Fe]_{LMC}}$
LMC	0.60	1
Fit *a*	< 0.72	< 1.2
Fit *b*	$0.18^{+2.3}_{-0.05}$	$0.3^{+0.11}_{-0.08}$
Fit *c*	$0.40^{+0.15}_{-0.13}$	$0.67^{+0.24}_{-0.22}$

Table 6.3: Abundance ratios of O and Fe

An ionization timescale in the order of $10^{11}s/cm^3$ indicates that the SNR is in Sedov phase. With the radii from the images and the estimated normalization factor, the mass of the X-ray emitting region, the age of the remnant and the shock velocity were calculated (Leahy et al. [2024]). The radius R is given by

$$R = D \cdot \tan(\theta)\text{pc} \tag{6.1}$$

where R is the radius in parsecs, D is the distance in parsecs, and θ is the angular size in radians. The distance to LMC is 49.59 ± 0.09(statistical) $\pm$ 0.54(systematic) kpc (Pietrzyński et al. [2019]). So, $D = 49.59 \pm 0.63$ is taken for the calculations.

The normalisation factor K is given by

$$K = \frac{10^{-14}}{4\pi D^2} \cdot \int n_e \, n_H \, dV \tag{6.2}$$

where $\int n_e \, n_H \, dV$ is the emission measure. Therefore, the emission measure EM is given by

$$EM = K \cdot \left(4\pi D^2\right) \cdot 10^{14}\text{cm}^{-6}. \tag{6.3}$$

Now, the ambient hydrogen density is estimated using the ratio of the electronic density to the ambient hydrogen density $\frac{n_e}{n_H} = 1.21$ (Warth,

SNR	O	Fe	O/Fe
	Type Ia		
J0508-6830	0^c	> 1.1	-
J0508-6902[b]	0^c	> 2.01	–
J0511-6759	0^c	11.4	-
J0534-6955	0.14 ± 0.01	3.4	0.41
J0534-7033	–	1.26	–
J0547-6941	$0.26^{+0.15}_{-0.28}$	2.3	0.11
	CC		
J0526-6605	0.30	0.41	0.73
J0535-6602	0.23	0.28	82
J0536-6735	1.57	0.04	39.25
J0453-6829	0.17	0.28	0.61
J0506-7009[TW]	$0.21 < x < 4.20$	$1.86 < x < 5.82$	$0.13 < x < 0.72$

Table 6.4: O and Fe abundances ($X/X_\odot$) of various SNRs in the LMC. [b] Values from Bozzetto et al. [2022]. [TW] This work. Else, values from Maggi, P. et al. [2016]. [c]The abundance is pegged at zero.

Gabriele et al. [2014]). Also, the swept-up X-ray emitting mass M_x is calculated as (Pannuti et al. [2014])

$$M_x = f m_H n_H V_x. \tag{6.4}$$

The filling factor f is assumed to be unity and the volume V_x considered here is the volume of the X-ray emitting ellipsoid. m_H is the mass of the hydrogen nucleus, 1.67×10^{-24} g. We find that $M_x = (1.09 \pm 0.6) \times 10^{34}$ g, which is $(5.5 \pm 3)\, M_\odot$.

The age is given by

$$t = \left(\frac{R}{14 \cdot \left(\frac{E_0}{n}\right)^{1/5}} \right)^{\frac{5}{2}} \cdot 10^4 \text{years}. \tag{6.5}$$

We assume an initial explosion energy of $1 \cdot 10^{51}$ ergs. From the H I density contours of the LMC presented in Mathewson and Ford [1984], the location of the SNR in the LMC is expected to have an HI surface density less than $1 \cdot 10^{21}$ and above $4 \cdot 10^{20} \text{atoms}/\text{cm}^2$. Coherently, in the HI column density image of the LMC in Kim et al. [2003], where the intensity range is 0 to 6 $\times 10^{21} \mathrm{H-atom cm}^{-2}$, the location of the SNR has negligibly low counts. Therefore, a HI density of $1 \times 10^{20} \text{cm}^{-2}$ is assumed. Further, assuming a uniform distribution of this particle surface density over the thickness of 360 pc (1.111×10^{21}cm) (Kim et al. [1999]), which is the diameter of the shell, the ambient particle density is calculated as $n_{calc} = 0.9 \text{atoms}/\text{cm}^3$. But, Kim et al. [2003] calculates a mean ambient particle density $n_{Kim} = 2$. It is noted that the SNR is located further away from the centre of the super bubble, and that the diameter as the thickness is an over-estimate.

Now that we have the age t and the radius R, we can estimate the shock velocity using

$$v_s = \frac{2R}{5t} \tag{6.6}$$

where v_s is the shock velocity.

These results are tabulated in Table 6.5

Effective X-ray Radius	12.62 ± 2.345 pc
	$(3.89 \pm 0.779) \times 10^{19}$ cm
Semimajor Axis	15.33 ± 3.07 pc
	$(4.73 \pm 0.95) \times 10^{19}$ cm
Semiminor Axis	9.91 ± 1.98 pc
	$(3.06 \pm 0.61) \times 10^{19}$ cm
Volume (X-ray emitting region)	$(1.85 \pm 0.829) \times 10^{59}$ cm^3
Forward shock Radius	25 ± 5 pc
Emission Measure (EM)	$(4.23^{+0.01}_{-0.35}) \times 10^{56}$ cm^{-6}
Hydrogen Density (n_H)	0.035 ± 0.012 cm^{-3}
X-ray emitting mass	5.5 ± 3.08 M$_\odot$
Age ($n = 0.9$)	41000 ± 2000 years
Shock velocity ($n = 0.9$)	240 ± 50 km/s
Age ($n = 2.0$)	61000 ± 3000 years
Shock velocity ($n = 2.0$)	160 ± 33 km/s

Table 6.5: Characteristics of the SNR

6.3 The Environment

The SNR is located in a super giant shell tabulated as SGS4 in Kim et al. [2003]. In addition, it is located in the region mentioned as SGS LMC-8 in Meaburn [1980] (figure 6.7). To mark this SGS LMC-8 region in the Hα map, the NASA/IPAC Extragalactic Database was used to convert the B1950 coordinates to the J2000 coordinates. The dimensions of the SGS LMC-8 were given in parsecs, which were converted to degrees assuming that the authors would have used a distance of 50 kpc to the LMC. Also, the complete circle as in the figure *(red)* was not marked in Meaburn [1980], but an arc that would be a north-east segment on this circle. Meaburn [1980] identified this region as a potential supergiant shell as filaments were not detected around their complete circumferences. According to the SIMBAD catalog, there are interstellar media, H-II regions, molecular clouds, young stellar objects, white dwarf candidates and a post-AGB star candidate identified in the vicinity of the SNR (figure 6.8).

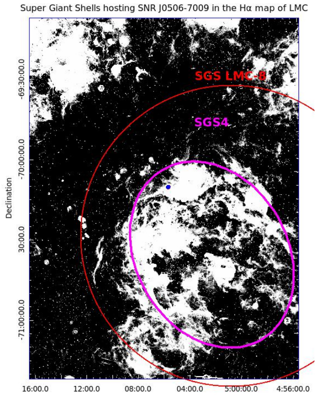

Figure 6.7: The Super Giant Shells hosting the remnant (blue).

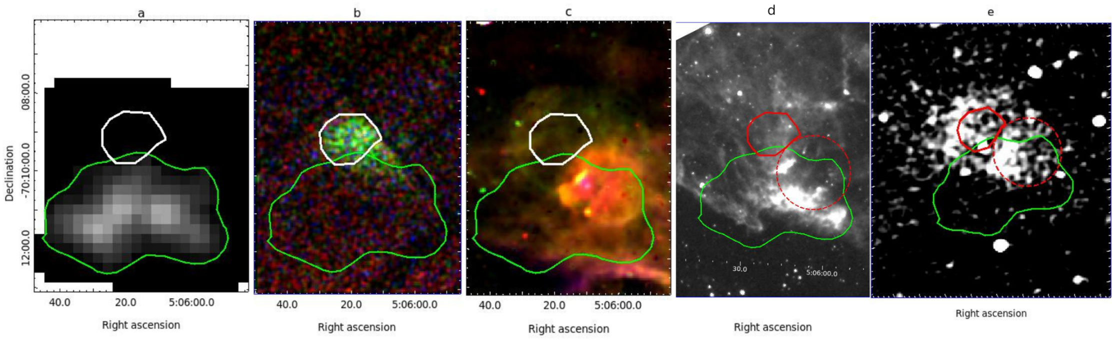

Figure 6.9: The molecular cloud complex indicated by CO intensity map. *a*: MAGMA CO integrated intensity. The regions of high CO intensity marked in (*b*) the three-color XMM-Newton image (R:$0.3-0.7$ keV; G:$0.7-1.1$ keV; B:$1.1-1.5$ keV),(*c*) in three-color MCELS image (R:Hα; G:[S II]; B:[O III]), (*d*) in IR map by SPITZER and (*e*) in radio continuum observed by ASKAP.

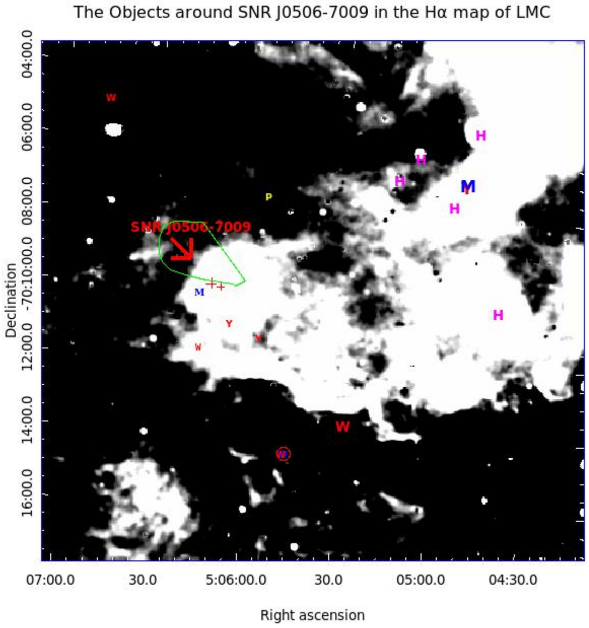

Figure 6.8: Objects around the remnant.

The red crosses towards the bottom of the green region are two ISMs, the blue M mark molecular clouds, the magenta H mark H-II regions, Y mark young stellar objects and the yellow P marks a post-AGB star candidate.

Analysing the MAGMA CO luminosity map indicates a region of high CO intensity near the SNR. This is marked in figure 6.9. It is likely that the SNR interacts with this dense region, as the boundaries of the X-ray ejecta and the CO intense cloud coincide. Fukui et al. [2008] lists a small molecular cloud at $\mathrm{RA} = 05^{\mathrm{h}}\,06^{\mathrm{m}}, \mathrm{Dec} = -70^{\circ}\,10'$ (J2000.0). The X-ray morphology of an SNR is believed to be affected by the interaction with dense clouds (Rho and Petre [1998]). The X-ray emission and the CO intensity contours (Fig 6.9) agree to this influence. Optical emission with low S II/Hα correlates only with the absence of X-rays in the south-west of the remnant's X-ray emission (Figure 6.2), where this molecular cloud is reported. In the MCELS three-colour composite image, we see a circular region at this location. It is interesting how the region of high Hα emission coincides with a dense molecular cloud.

6.4 Typing of the SNR

The metal abundances, morphology and neighbourhood are important indicators of the type of the explosion. Here, the [Fe] abundance and [O]/[Fe] abundance ratios favor a Type 1a explosion. The estimated x-ray emitting mass also supports this possibility. However, the mass estimate from the fit with its wider range of uncertainty inhibits from making a conclusive statement.

The molecular cloud complex hinted by intense CO emission lines and IR data by SPITZER shows spatial anti-correlation with the SNR. The proximity of a molecular cloud indicates a CC scenario (Slane et al. [2016]; Makarenko et al. [2023]). Jiang et al. [2010] lists 64 galactic SNRs (34 confirmed ones, 11 probable ones with strong evidence but not conclusive yet, and 19 possible ones yet to be determined with further observations) that are in physical contact with MCs, of which only one is a known Type Ia SNR.

The X-ray emitting source region is nearly circular and mirror-symmetric. This can be seen in the X-ray image produced by combining only mos1 and mos2 detectors, as the edge of the source falls in the chip gap of the pn detector. Peters et al. [2013] infers statistically that Type Ia SNRs are more circular and mirror symmetric than the CC SNRs. However, there are many counterexamples to this pattern. The spatial anti-correlation with the clouds hints at a possible interaction between the clouds and the remnant, and this could have significantly affected the shape of the remnant.

In the optical images (Figure 6.2), near the x-ray emitting SNR region, centered at $\mathrm{RA} = 05^{\mathrm{h}}\,06^{\mathrm{m}}$, $\mathrm{Dec} = -70^{\circ}\,10'$ (J2000.0), a unique region is seen (Figure 7.1). This can be seen as a dark circle in the $\mathrm{S\,II}/\mathrm{H}\,\alpha$ image (Fig. 6.2 (b)) or as an orange circular region in the MCELS composite RGB image (Fig. 6.2 (a)). The author found this interesting to investigate into what is happening in this region, calling it region SW (Figure 7.1).

CHAPTER 7

The Neighboring Region J0506-7010

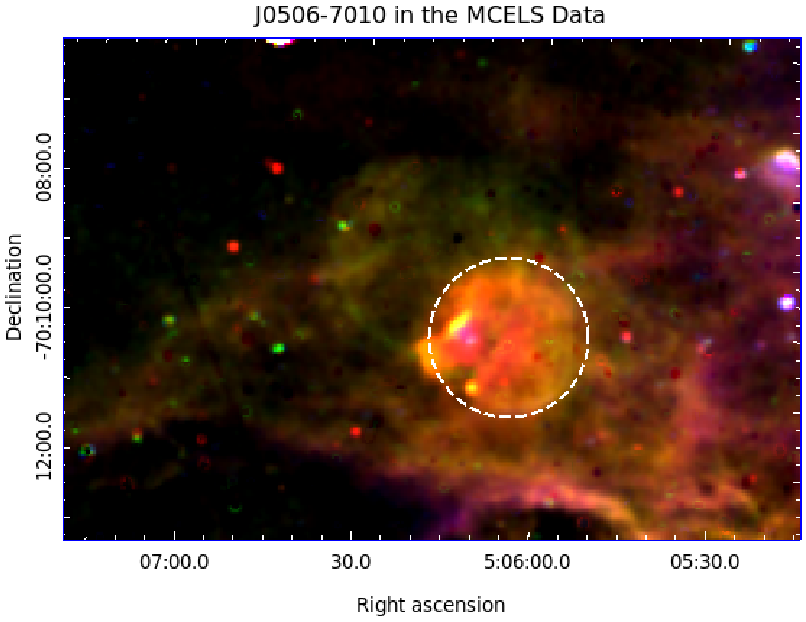

Figure 7.1: Region SW in the MCELS three-color image.

The first assumption about the region SW was that it is masking the x-ray emission from the 'tail' of the SNR, as we see still fainter x-ray emission in region b (Figure 7.2). With high Hα emission, this could be an H II region. By assuming the distance to this object to be the distance to the LMC (49.59 ± 0.63 kpc), the radius, and the shape to be spherical, the volume are estimated and listed in Table 7.1.

Radius	16.44 ± 3.29 pc
	$(5.07 \pm 1.01) \times 10^{19}$ cm
Volume	$(5.47 \pm 2.45) \times 10^{59}$ cm^3

Table 7.1: Radius and Volume of the Orange object

This region SW has no peculiar x-ray emission in the XMM-Newton observation, but apparently a portion of the SNR's x-ray emission is covered by this region. This region, the region b (Fig 7.2), is studied for its

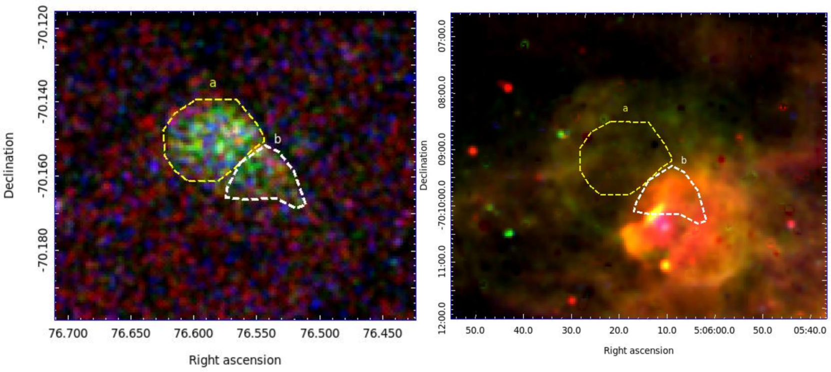

Figure 7.2: The regions from which the x-ray spectra were analysed, marked in the three-color images of XMM-Newton (left) and MCELS (right).

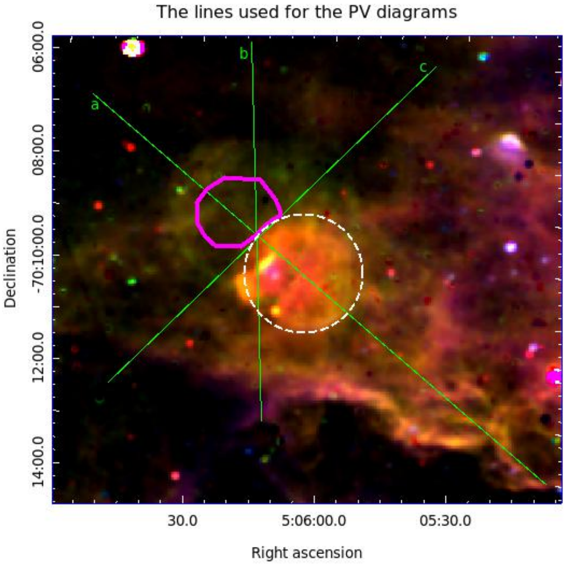

Figure 7.3: The lines along which the PV diagrams were generated for the region SW.

x-ray emission, freezing the parameters to the fitted values of region a (fit (c)), except the absorbing hydrogen density, N_H, of the *xspec* model `TBVarabs`. The hydrogen densities of both regions are compared in Table 7.2. The difference in the absorbing Hydrogen density, ΔN_H, estimated to be $(0.8 \pm 0.1) \cdot 10^{22}$ cm^{-2}, indicates the higher hydrogen density of the small region in the orange object. Although the hydrogen density of an H II region need not necessarily be uniform, this hints at the Hydrogen density of the region SW region. Table 7.2 also shows that the x-ray luminosity is affected by the region SW. These suggest that the region SW is dense in Hydrogen and is positioned in front of the SNR. This region was further investigated by using the published H I velocity data from Kim et al. [2003] observed with ATCA and Parkes telescope. The position-velocity (PV) diagrams of this region was generated to check for characteristic gaps or cavities (Figure 7.4). The lines along which the PV diagrams are generated are shown in Figure 7.3. No characteristic signatures of an H II region was observed in this data cube, refuting the possibility of the region SW being an H II region.

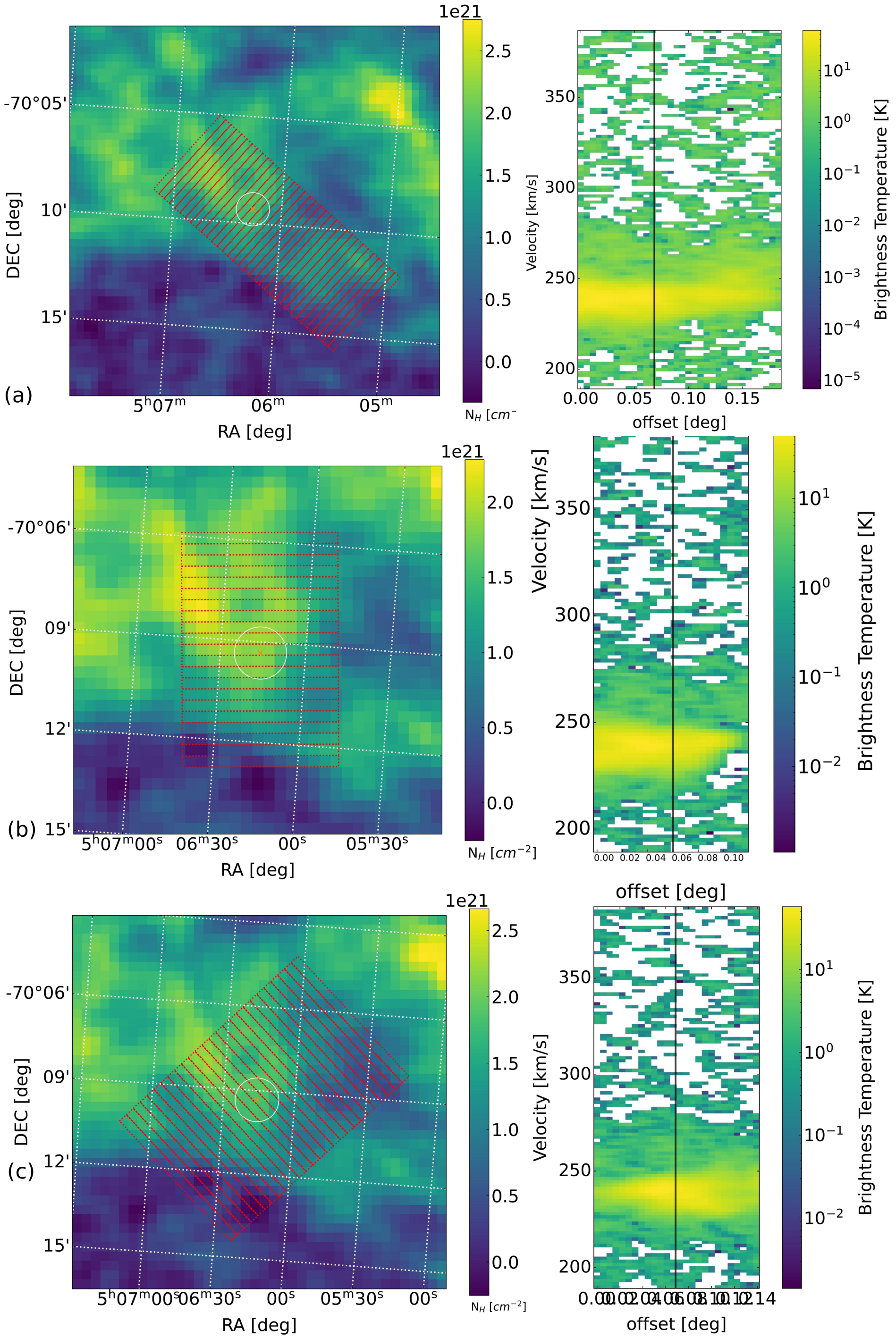

Figure 7.4: The PV diagrams of the region SW generated from the H I Parkes data.

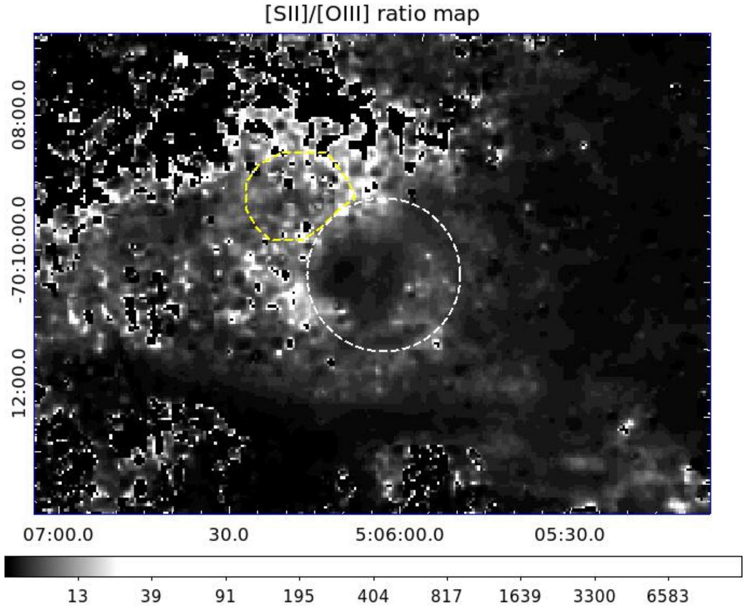

Figure 7.5: The ionisation structure shown by the [S II]/[O III] ratio.

Pellegrini et al. [2012] present a modern development, demonstration and application of ionisation parameter mapping (IPM) to assess the optical depth of H II regions. A low [S II/O III] ratio indicates highly ionised medium and a high [S II/O III] ratio indicates a sharp transition in the ionisation. Figure 7.5 shows the continuum subtracted *log* [S II/O III] ratio map of this region. This ionisation structure reveals that the region SW is ionised and a partial shell of sharp ionisaton transition. However, this does not show a distinct structure and suggests negation to the possibility of region SW being an H II region.

Region	Luminosity (10^{34} erg/s)			N_H (10^{22} cm^{-2})
	Unabsorbed	Absorbed	Difference ΔL	
a	$1.25^{+0.00}_{-0.17}$	$1.05^{+0.00}_{-0.01}$	0.20	< 0.08
b	$2.01^{+0.00}_{-0.00}$	$0.70^{+0.01}_{-0.01}$	1.31	$0.88^{+0.10}_{-0.09}$
Difference	0.76	-0.35		0.8 ± 0.1

Table 7.2: Luminosities and equivalent H densities of regions a and b

Two massive stars and three young stellar objects (YSOs) were found in this region (Fig 7.6). One YSO was outside the region, but quite close. These are the two stars seen between the evolutionary tracks of 7 and 9 M$_\odot$ in the color magnitude diagram (CMD) (Fig 7.7) plotted on the stellar population from Zaritsky et al. [2004]. This CMD was plotted using the MESA Isochrones and Stellar Tracks (MIST) (Dotter [2016]; Choi et al. [2016]; Paxton et al. [2011]; Paxton et al. [2013]; Paxton et al. [2015]). With this number of existing massive stars, the initial mass function (Fig 7.8) was estimated using the Salpeter model (Salpeter [1955]) and thus the star formation history (SFH) too. The SFH reveals the existence of three massive stars (> 8 M$_\odot$) in this region. These numbers reinstate the possibility of this region being an H II region.

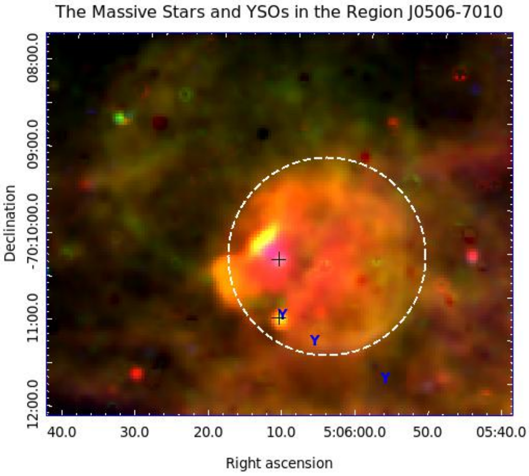

Figure 7.6: The massive stars (black cross) and YSOs (blue Y) in the region SW marked in the three-color image from the MCELS data, a superposition of Hα emission in red, [S II] in green and [O III] in blue.

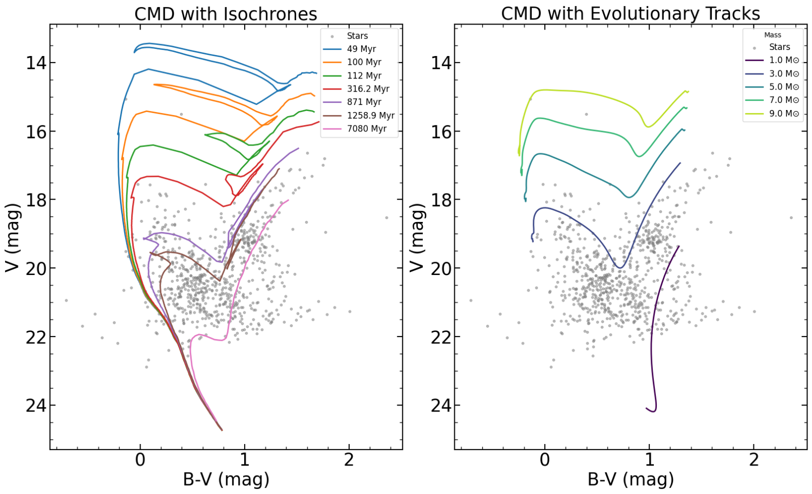

Figure 7.7: Left: CMD with Geneva isochrones ($Z = 0.008$). Right: CMD with MIST evolutionary tracks (1–9 $M_{\odot}$).

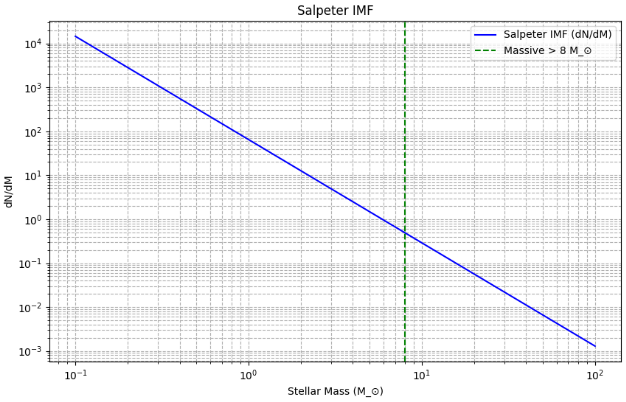

Figure 7.8: IMF fitted to the Salpeter model ($\mathrm{d}N/\mathrm{d}M \propto M^{-2.35}$).

CHAPTER 8

Summary, Conclusion & Outlook

The motivation of this thesis was primarily to get a better understanding of the X-ray loud object at $\mathrm{RA} = 05^{\mathrm{h}}\,06^{\mathrm{m}}, \mathrm{Dec} = -70^{\circ}\,09'$ (J2000.0), which was confirmed by Zangrandi et al. [2024] as a SNR. The S II/H α ratio confirms the region is shocked (Chapter 6). The main part of this thesis is the XMM-Newton analysis of the remnant (Chapter 5,6). The X-ray spectra was modeled with various XSPEC models where the ejecta was modeled using *vnei* model. The fit reveals a thermally ionised plasma and an Iron abundance higher than the average value for the LMC (Chapter 6). A comparison with the optical images estimates it to be old (41000 ± 2000 years). The age, shock velocity (240 ± 50 km/s), ionisation time-scale ($\gtrsim 1 \times 10^{11}$ s/cm^3) and radio emission suggests that the remnant is likely at the end of the Sedov phase (Woltjer [1972]). The calculations hint that the progenitor star was likely massive. The metal abundance ratios favor a core-collapse scenario for the origin of the remnant. An X-ray observation with a higher resolution that can better constrain the metal abundances, particularly, the abundances of Fe with O, Mg or any other alpha elements, can be useful in securely typing the remnant.

The H α emission map suggests an H II region neighbouring the remnant. This region was investigated using the H I map and [S II]/[O III] ratio map, both of them refuted the possibility of this structure being an H II region. The X-ray data and fit suggests that this structure is absorbing the X-ray emission from the remnant. Further, a color magnitude diagram was plotted for this region and the IMF estimated. These suggest the existence of three massive stars, two of which are still alive (Chapter 7). A detailed analysis of this region will help to confirm if this is an H II region or not. The proximity of the likely H II region along with proximal massive stars favors a core-collapse scenario. A detailed study of this region in the IR and a better understanding of the dust and the magnetohydrodynamics of this region will be insightful.

MAGMA data suggests a molecular cloud having apparent spatial anti-correlation with the X-ray ejecta of the SNR (section 6.3). This proximity also favors a core-collapse scenario. It is highly likely that the X-ray morphology was shaped by interaction with this cloud complex. An observation of this region in higher energies (γ rays) can show if particles are accelerated at this shock front, and confirm the interaction. Or an X-ray observation with good sensitivity in the > 6 keV range can tell us about non-thermal X-rays which we expect in an SNR-MC interaction. Suzuki et al. [2024] and Morikawa et al. [2025] proposes that the interaction of particles formed in the SNR shell with clouds can result in a neutral iron line emission at 6.4 keV. Also, OH maser emission line at 1720 MHz can be a tracer of the remnant's shock expanding into the molecular cloud (Yusef-Zadeh et al. [2003]).

With a bright H α region, a molecular cloud complex, YSOs and massive stars nearby, and being in a superbubble, a detailed study of the interactions around this SNR alone can tell us significantly more about how influential a star is. In essence, the field-of-view of this XMM-Newton observation is particularly interesting, but the resolution was limiting. A detailed multi-messenger analysis can give us a significantly better understanding of the universe.

Bibliography

Ling-Xiao Dang, Ping Zhou, Lei Sun, Junjie Mao, Jacco Vink, Qian-Qian Zhang, and Vladimír Domček. Typing supernova remnant g352.7-0.1 using xmm–newton x-ray observations. *Monthly Notices of the Royal Astronomical Society*, 529(4):4117–4127, March 2024. ISSN 1365-2966. doi: 10.1093/mnras/stae805. URL http://dx.doi.org/10.1093/mnras/stae805.

D. S. Mathewson and J. R. Healey. Continuum radio emission from the magellanic clouds. *Symposium - International Astronomical Union*, 20:245–255, 1964. doi: 10.1017/S0074180900052669.

Nausicaa Delmotte. The Large Magellanic Cloud as a testbed for the astronomical virtual observatory. In Peter J. Quinn and Alan Bridger, editors, *Optimizing Scientific Return for Astronomy through Information Technologies*, volume 5493 of *Society of Photo-Optical Instrumentation Engineers (SPIE) Conference Series*, pages 277–285, September 2004. doi: 10.1117/12.550504.

G. Pietrzyński, D. Graczyk, A. Gallenne, W. Gieren, I. B. Thompson, B. Pilecki, P. Karczmarek, M. Górski, K. Suchomska, M. Taormina, B. Zgirski, P. Wielgórski, Z. Kołaczkowski, P. Konorski, S. Villanova, N. Nardetto, P. Kervella, F. Bresolin, R. P. Kudritzki, J. Storm, R. Smolec, and W. Narloch. A distance to the large magellanic cloud that is precise to one per cent. *Nature*, 567(7747):200–203, March 2019. ISSN 1476-4687. doi: 10.1038/s41586-019-0999-4. URL http://dx.doi.org/10.1038/s41586-019-0999-4.

G. Robert Brakenridge. Late Quaternary supernovae in Earth history. , 539(4): 3201–3219, June 2025. doi: 10.1093/mnras/staf554.

Dina Prialnik. *An Introduction to the Theory of Stellar Structure and Evolution*. 2009.

D. Buhl. Molecular clouds in the galaxy. *Proceedings of the IEEE*, 61(9):1198–1204, 1973. doi: 10.1109/PROC.1973.9245.

M. Chevance, J. M. D. Kruijssen, and E. andensemblename=et al. Vazquez-Semadeni. The molecular cloud lifecycle. *Space Science Reviews*, 216(50), 2020. doi: 10.1007/s11214-020-00674-x.

A. P. S. Hygate. *The Physics of Cloud-scale Star Formation and Feedback Across Cosmic Time*. Dissertation, Zentrum für Astronomie der Universität Heidelberg (ZAH), 2020.

Ralf S. Klessen, Andreas Burkert, and Matthew R. Bate. Fragmentation of Molecular Clouds: The Initial Phase of a Stellar Cluster. , 501(2):L205–L208, July 1998. doi: 10.1086/311471.

M. Saberi, W. H. T. Vlemmings, and E. De Beck. Photodissociation of CO in the outflow of evolved stars. , 625:A81, May 2019. doi: 10.1051/0004-6361/201935309.

T. M. Dame, Dap Hartmann, and P. Thaddeus. The Milky Way in Molecular Clouds: A New Complete CO Survey. , 547(2):792–813, February 2001. doi: 10.1086/318388.

Desika Narayanan, Mark R. Krumholz, Eve C. Ostriker, and Lars Hernquist. A general model for the co–h2 conversion factor in galaxies with applications to the star formation law. *Monthly Notices of the Royal Astronomical Society*, 421 (4):3127–3146, 04 2012. ISSN 0035-8711. doi: 10.1111/j.1365-2966.2012.20536.x. URL https://doi.org/10.1111/j.1365-2966.2012.20536.x.

F. P. Israel. H_2 and its relation to CO in the LMC and other magellanic irregular galaxies. , 328:471–482, December 1997. doi: 10.48550/arXiv.astro-ph/9709194.

V. Lebouteiller, D. Cormier, S. C. Madden, M. Galametz, S. Hony, F. Galliano, M. Chevance, M. Y. Lee, J. Braine, F. L. Polles, M. A. Requeña-Torres, R. Indebetouw, A. Hughes, and N. Abel. Physical conditions in the gas phases of the giant H II region LMC-N 11. II. Origin of [C II] and fraction of CO-dark gas. , 632:A106, December 2019. doi: 10.1051/0004-6361/201936303.

Ekaterina I Makarenko, Stefanie Walch, Seamus D Clarke, Daniel Seifried, Thorsten Naab, Pierre C Nürnberger, and Tim-Eric Rathjen. How do supernova remnants cool? – i. morphology, optical emission lines, and shocks. *Monthly Notices of the Royal Astronomical Society*, 523(1):1421–1440, May 2023. ISSN 1365-2966. doi: 10.1093/mnras/stad1472. URL http://dx.doi.org/10.1093/mnras/stad1472.

Y. L. Huang and P. Thaddeus. Molecular Clouds and Supernova Remnants in the Outer Galaxy. , 309:804, October 1986. doi: 10.1086/164649.

Xin Zhou, Yang Su, Ji Yang, Xuepeng Chen, Yan Sun, Zhibo Jiang, Min Wang, Hongchi Wang, Shaobo Zhang, Ye Xu, Qingzeng Yan, Lixia Yuan, Zhiwei Chen, Yiping Ao, and Yuehui Ma. A systematic study of associations between supernova remnants and molecular clouds, 2023. URL https://arxiv.org/abs/2308.03484.

Bing Jiang, Yang Chen, Junzhi Wang, Yang Su, Xin Zhou, Samar Safi-Harb, and Tracey DeLaney. Cavity of Molecular Gas Associated with Supernova Remnant 3C 397. , 712(2):1147–1156, April 2010. doi: 10.1088/0004-637X/712/2/1147.

F. Aharonian, A. G. Akhperjanian, A. R. Bazer-Bachi, B. Behera, M. Beilicke, W. Benbow, D. Berge, K. Bernlöhr, C. Boisson, O. Bolz, V. Borrel, I. Braun, E. Brion, A. M. Brown, R. Bühler, T. Bulik, I. Büsching, T. Boutelier, S. Carrigan, P. M. Chadwick, L. M. Chounet, A. C. Clapson, G. Coignet, R. Cornils, L. Costamante, B. Degrange, H. J. Dickinson, A. Djannati-Ataï, W. Domainko, L. O'C. Drury, G. Dubus, J. Dyks, K. Egberts, D. Emmanoulopoulos, P. Espigat, C. Farnier, F. Feinstein, A. Fiasson, A. Förster, G. Fontaine, Y. Fukui, Seb. Funk, S. Funk, M. Füßling, Y. A. Gallant, B. Giebels, J. F. Glicenstein, B. Glück, P. Goret, C. Hadjichristidis, D. Hauser, M. Hauser, G. Heinzelmann, G. Henri, G. Hermann, J. A. Hinton, A. Hoffmann, W. Hofmann, M. Holleran,

S. Hoppe, D. Horns, A. Jacholkowska, O. C. de Jager, E. Kendziorra, M. Kerschhaggl, B. Khélifi, Nu. Komin, K. Kosack, G. Lamanna, I. J. Latham, R. Le Gallou, A. Lemière, M. Lemoine-Goumard, J. P. Lenain, T. Lohse, J. M. Martin, O. Martineau-Huynh, A. Marcowith, C. Masterson, G. Maurin, T. J. L. McComb, R. Moderski, Y. Moriguchi, E. Moulin, M. de Naurois, D. Nedbal, S. J. Nolan, J. P. Olive, K. J. Orford, J. L. Osborne, M. Ostrowski, M. Panter, G. Pedaletti, G. Pelletier, P. O. Petrucci, S. Pita, G. Pühlhofer, M. Punch, S. Ranchon, B. C. Raubenheimer, M. Raue, S. M. Rayner, O. Reimer, M. Renaud, J. Ripken, L. Rob, L. Rolland, S. Rosier-Lees, G. Rowell, B. Rudak, J. Ruppel, V. Sahakian, A. Santangelo, L. Saugé, S. Schlenker, R. Schlickeiser, R. Schröder, U. Schwanke, S. Schwarzburg, S. Schwemmer, A. Shalchi, H. Sol, D. Spangler, Ł. Stawarz, R. Steenkamp, C. Stegmann, G. Superina, T. Takeuchi, P. H. Tam, J. P. Tavernet, R. Terrier, C. van Eldik, G. Vasileiadis, C. Venter, J. P. Vialle, P. Vincent, M. Vivier, H. J. Völk, F. Volpe, S. J. Wagner, and M. Ward. Discovery of very high energy gamma-ray emission coincident with molecular clouds in the W 28 (G6.4-0.1) field. , 481(2):401–410, April 2008. doi: 10.1051/0004-6361:20077765.

A. A. Abdo, M. Ackermann, M. Ajello, A. Allafort, L. Baldini, J. Ballet, G. Barbiellini, D. Bastieri, K. Bechtol, R. Bellazzini, B. Berenji, R. D. Blandford, E. D. Bloom, E. Bonamente, A. W. Borgland, A. Bouvier, T. J. Brandt, J. Bregeon, M. Brigida, P. Bruel, R. Buehler, S. Buson, G. A. Caliandro, R. A. Cameron, P. A. Caraveo, S. Carrigan, J. M. Casandjian, C. Cecchi, Ö. Çelik, A. Chekhtman, J. Chiang, S. Ciprini, R. Claus, J. Cohen-Tanugi, J. Conrad, C. D. Dermer, F. de Palma, E. do Couto e Silva, P. S. Drell, R. Dubois, D. Dumora, C. Farnier, C. Favuzzi, S. J. Fegan, Y. Fukazawa, Y. Fukui, S. Funk, P. Fusco, F. Gargano, N. Gehrels, S. Germani, N. Giglietto, F. Giordano, T. Glanzman, G. Godfrey, I. A. Grenier, J. E. Grove, S. Guiriec, D. Hadasch, Y. Hanabata, A. K. Harding, E. Hays, D. Horan, R. E. Hughes, G. Jóhannesson, A. S. Johnson, W. N. Johnson, T. Kamae, H. Katagiri, J. Kataoka, J. Knödlseder, M. Kuss, J. Lande, L. Latronico, S.-H. Lee, M. Lemoine-Goumard, M. Llena Garde, F. Longo, F. Loparco, M. N. Lovellette, P. Lubrano, A. Makeev, M. N. Mazziotta, P. F. Michelson, W. Mitthumsiri, T. Mizuno, A. A. Moiseev, C. Monte, M. E. Monzani, A. Morselli, I. V. Moskalenko, S. Murgia, T. Nakamori, P. L. Nolan, J. P. Norris, E. Nuss, M. Ohno, T. Ohsugi, N. Omodei, E. Orlando, J. F. Ormes, M. Ozaki, J. H. Panetta, D. Parent, V. Pelassa, M. Pepe, M. Pesce-Rollins, F. Piron, T. A. Porter, S. Rainò, R. Rando, M. Razzano, A. Reimer, O. Reimer, T. Reposeur, A. Y. Rodriguez, M. Roth, H. F.-W. Sadrozinski, A. Sander, P. M. Saz Parkinson, C. Sgrò, E. J. Siskind, D. A. Smith, P. D. Smith, G. Spandre, P. Spinelli, M. S. Strickman, D. J. Suson, H. Tajima, H. Takahashi, T. Takahashi, T. Tanaka, J. B. Thayer, J. G. Thayer, D. J. Thompson, L. Tibaldo, O. Tibolla, D. F. Torres, G. Tosti, Y. Uchiyama, T. Uehara, T. L. Usher, V. Vasileiou, N. Vilchez, V. Vitale, A. P. Waite, P. Wang, B. L. Winer, K. S. Wood, H. Yamamoto, R. Yamazaki, Z. Yang, T. Ylinen, and M. Ziegler. Fermilarge area telescope observations of the supernova remnant w28 (g6.4–0.1). *The Astrophysical Journal*, 718(1):348–356, June 2010. ISSN 1538-4357. doi: 10.1088/0004-637x/718/1/348. URL http://dx.doi.org/10.1088/0004-637X/718/1/348.

Duncan Forgan and Ken Rice. The jeans mass as a fundamental measure of self-gravitating disc fragmentation and initial fragment mass. *Monthly Notices of the Royal Astronomical Society*, 417(3):1928–1937, 10 2011. ISSN 0035-8711. doi: 10.1111/j.1365-2966.2011.19380.x. URL https://doi.org/10.1111/j.1365-2966.2011.19380.x.

Frederick D. Seward and Philip A. Charles. *Exploring the X-ray Universe*. 2010.

Jacco Vink. Supernova remnants: the X-ray perspective. , 20:49, December 2012. doi: 10.1007/s00159-011-0049-1.

Ke-Jung Chen, Alexander Heger, Stan Woosley, Ann Almgren, and Daniel J. Whalen. Pair instability supernovae of very massive population iii stars. *The Astrophysical Journal*, 792(1):44, August 2014. ISSN 1538-4357. doi: 10.1088/0004-637x/792/1/44. URL http://dx.doi.org/10.1088/0004-637X/792/1/44.

D. Whalen, Muhammad Latif, and C. Jessop. Abundant water from primordial supernovae at cosmic dawn. *Nature Astronomy*, 9:741–746, 03 2025. doi: 10.1038/s41550-025-02479-w.

M. Ackermann, M. Ajello, A. Allafort, L. Baldini, J. Ballet, G. Barbiellini, M. G. Baring, D. Bastieri, K. Bechtol, R. Bellazzini, R. D. Blandford, E. D. Bloom, E. Bonamente, A. W. Borgland, E. Bottacini, T. J. Brandt, J. Bregeon, M. Brigida, P. Bruel, R. Buehler, G. Busetto, S. Buson, G. A. Caliandro, R. A. Cameron, P. A. Caraveo, J. M. Casandjian, C. Cecchi, Ö. Çelik, E. Charles, S. Chaty, R. C. G. Chaves, A. Chekhtman, C. C. Cheung, J. Chiang, G. Chiaro, A. N. Cillis, S. Ciprini, R. Claus, J. Cohen-Tanugi, L. R. Cominsky, J. Conrad, S. Corbel, S. Cutini, F. D'Ammando, A. de Angelis, F. de Palma, C. D. Dermer, E. do Couto e Silva, P. S. Drell, A. Drlica-Wagner, L. Falletti, C. Favuzzi, E. C. Ferrara, A. Franckowiak, Y. Fukazawa, S. Funk, P. Fusco, F. Gargano, S. Germani, N. Giglietto, P. Giommi, F. Giordano, M. Giroletti, T. Glanzman, G. Godfrey, I. A. Grenier, M. H. Grondin, J. E. Grove, S. Guiriec, D. Hadasch, Y. Hanabata, A. K. Harding, M. Hayashida, K. Hayashi, E. Hays, J. W. Hewitt, A. B. Hill, R. E. Hughes, M. S. Jackson, T. Jogler, G. Jóhannesson, A. S. Johnson, T. Kamae, J. Kataoka, J. Katsuta, J. Knödlseder, M. Kuss, J. Lande, S. Larsson, L. Latronico, M. Lemoine-Goumard, F. Longo, F. Loparco, M. N. Lovellette, P. Lubrano, G. M. Madejski, F. Massaro, M. Mayer, M. N. Mazziotta, J. E. McEnery, J. Mehault, P. F. Michelson, R. P. Mignani, W. Mitthumsiri, T. Mizuno, A. A. Moiseev, M. E. Monzani, A. Morselli, I. V. Moskalenko, S. Murgia, T. Nakamori, R. Nemmen, E. Nuss, M. Ohno, T. Ohsugi, N. Omodei, M. Orienti, E. Orlando, J. F. Ormes, D. Paneque, J. S. Perkins, M. Pesce-Rollins, F. Piron, G. Pivato, S. Rainò, R. Rando, M. Razzano, S. Razzaque, A. Reimer, O. Reimer, S. Ritz, C. Romoli, M. Sánchez-Conde, A. Schulz, C. Sgrò, P. E. Simeon, E. J. Siskind, D. A. Smith, G. Spandre, P. Spinelli, F. W. Stecker, A. W. Strong, D. J. Suson, H. Tajima, H. Takahashi, T. Takahashi, T. Tanaka, J. G. Thayer, J. B. Thayer, D. J. Thompson, S. E. Thorsett, L. Tibaldo, O. Tibolla, M. Tinivella, E. Troja, Y. Uchiyama, T. L. Usher, J. Vandenbroucke, V. Vasileiou, G. Vianello, V. Vitale, A. P. Waite, M. Werner, B. L. Winer, K. S. Wood, M. Wood, R. Yamazaki, Z. Yang, and S. Zimmer. Detection of the Characteristic Pion-Decay Signature in Supernova Remnants. *Science*, 339(6121):807–811, February 2013. doi: 10.1126/science.1231160.

G. Giuliani and AGILE Team. AGILE observations of Middle-aged supernova remnants. , 82:747, January 2011.

Iurii Sushch, Pasquale Blasi, and Robert Brose. Supernova remnants in super bubbles as cosmic ray accelerators. *arXiv e-prints*, art. arXiv:2505.02523, May 2025. doi: 10.48550/arXiv.2505.02523.

D. Onić, D. Urošević, B. Arbutina, and D. Leahy. On the Existence of "Radio Thermally Active" Galactic Supernova Remnants. , 756(1):61, September 2012. doi: 10.1088/0004-637X/756/1/61.

H. Sano, S. Yoshiike, Y. Yamane, K. Hayashi, R. Enokiya, K. Tokuda, K. Tachihara, G. Rowell, M. D. Filipović, and Y. Fukui. Alma co observations of the mixed-morphology supernova remnant w49b: Efficient production of recombining plasma and hadronic gamma rays via shock–cloud interactions. *The Astrophysical Journal*, 919(2):123, October 2021. ISSN 1538-4357. doi: 10.3847/1538-4357/ac0dba. URL http://dx.doi.org/10.3847/1538-4357/ac0dba.

Daniel Rouan. *HII Region*, pages 705–705. Springer Berlin Heidelberg, Berlin, Heidelberg, 2011. ISBN 978-3-642-11274-4. doi: 10.1007/978-3-642-11274-4_723. URL https://doi.org/10.1007/978-3-642-11274-4_723.

R. C. Kennicutt and P. W. Hodge. H II regions in NGC 628. III - H-alpha luminosities and the luminosity function. , 241:573–586, October 1980. doi: 10.1086/158372.

Leticia Carigi, Manuel Peimbert, and Antonio Peimbert. The last 5 gyr of galactic chemical evolution based on h ii region abundances derived from a temperature independent method. *The Astrophysical Journal*, 873(2):107, mar 2019. doi: 10.3847/1538-4357/aaf28e. URL https://dx.doi.org/10.3847/1538-4357/aaf28e.

H. Friedman, S. W. Lichtman, and E. T. Byram. Photon counter measurements of solar x-rays and extreme ultraviolet light. *Phys. Rev.*, 83:1025–1030, Sep 1951. doi: 10.1103/PhysRev.83.1025. URL https://link.aps.org/doi/10.1103/PhysRev.83.1025.

Riccardo Giacconi, Herbert Gursky, Frank R. Paolini, and Bruno B. Rossi. Evidence for x rays from sources outside the solar system. *Phys. Rev. Lett.*, 9:439–443, Dec 1962. doi: 10.1103/PhysRevLett.9.439. URL https://link.aps.org/doi/10.1103/PhysRevLett.9.439.

R. Giacconi, H. Gursky, and J. R. Waters. Two sources of cosmic x-rays in scorpius and sagittarius. *Nature*, 204:981–982, December 1964. doi: 10.1038/204981a0.

N. Jagoda, G. Austin, S. Mickiewicz, and R. Goddard. The uhuru x-ray instrument. *IEEE Transactions on Nuclear Science*, 19:579–, February 1972.

K. Arnaud, R. Smith, and A. Siemiginowska. *Handbook of X-ray Astronomy*. Cambridge University Press, November 2011.

R. Giacconi. The Einstein X-ray Observatory. *Scientific American*, 242:80–85, February 1980. doi: 10.1038/scientificamerican0280-80.

J. Trümper. The rosat mission. *Advances in Space Research*, 2:241–249, 1982. doi: 10.1016/0273-1177(82)90070-9.

R. Staubert. *Aperture Modulation Telescopes*, pages 29–39. Springer Berlin Heidelberg, Berlin, Heidelberg, 2008. ISBN 978-3-540-34412-4. doi: 10.1007/978-3-540-34412-4_5. URL https://doi.org/10.1007/978-3-540-34412-4_5.

C. Reppin, W. Pietsch, J. Trümper, E. Kendziorra, and R. Staubert. High Energy X-ray Experiment for the Saljut-Mission (HEXE). In G. C. Perola and M. Salvati, editors, *Non-thermal and Very High Temperature Phenomena in X-ray Astronomy*, page 279. 1985.

Hans Wolter. Spiegelsysteme streifenden Einfalls als abbildende Optiken für Röntgenstrahlen. *Annalen der Physik*, 445(1):94–114, January 1952. doi: 10.1002/andp.19524450108.

M. C. Weisskopf, B. Brinkman, C. Canizares, G. Garmire, S. Murray, and L. P. Van Speybroeck. An Overview of the Performance and Scientific Results from the Chandra X-Ray Observatory. , 114(791):1–24, January 2002. doi: 10.1086/338108.

F. Jansen, D. Lumb, B. Altieri, J. Clavel, M. Ehle, C. Erd, C. Gabriel, M. Guainazzi, P. Gondoin, R. Much, R. Munoz, M. Santos, N. Schartel, D. Texier, and G. Vacanti. XMM-Newton observatory. I. The spacecraft and operations. , 365:L1–L6, January 2001. doi: 10.1051/0004-6361:20000036.

W. C. Röntgen. Über eine neue art von strahlen. *Sitzungsberichte der Physikalisch-medicinischen Gesellschaft zu Würzburg*, 95, 1895.

E. Rutherford and H. Geiger. An electrical method of counting the number of α particles from radioactive substances. *Proceedings of the Royal Society of London. Series A, Containing Papers of a Mathematical and Physical Character*, 81:141–161, 1908. doi: 10.1098/rspa.1908.0065.

E. Pfeffermann. Proportional counters. In J. E. Trümper and G. Hasinger, editors, *The Universe in X-rays*, pages 5–14. Springer, Berlin, Heidelberg, 2008. doi: 10.1007/978-3-540-34412-4_2.

E. Kendziorra. Gas scintillation proportional counters. In J. E. Trümper and G. Hasinger, editors, *The Universe in X-rays*, pages 15–19. Springer, Berlin, Heidelberg, 2008. doi: 10.1007/978-3-540-34412-4_3.

Subhajeet Karmakar and Allison Youngblood. Investigating X-ray flares on an active ultrafast rotator AB Dor using XMM-Newton. In *American Astronomical Society Meeting Abstracts*, volume 246 of *American Astronomical Society Meeting Abstracts*, page 128.08, June 2025.

Adriana Mancini Pires, Christian Motch, Axel Schwope, Iris Traulsen, Jean Ballet, Sudip Chakraborty, David Homan, Jan Kurpas, Ada Nebot Gomez-Moràn, François-Xavier Pineau, Hugo Tranin, and Natalie Webb. Isolated Neutron Stars as Science Validation for XMM2ATHENA: Ensuring Robust Data for Future X-Ray Astronomy. *Astronomische Nachrichten*, 346(3-4):e20240116, March 2025. doi: 10.1002/asna.20240116.

A. Avakyan, A. Zainab, V. Doroshenko, J. Wilms, A. Schwope, V. Suleimanov, D. Buckley, J. Brink, and A. Santangelo. XMM-Newton follow-up of two eROSITA X-ray binary candidates. *arXiv e-prints*, art. arXiv:2507.08592, July 2025.

N. La Palombara, L. Sidoli, S. Mereghetti, P. Esposito, and G. L. Israel. The persistent nature of the Be X-ray binary pulsar 4U 0728-25. , 696:A197, April 2025. doi: 10.1051/0004-6361/202554103.

A. Reguitti, A. Pastorello, S. J. Smartt, G. Valerin, G. Pignata, S. Campana, T. W. Chen, A. K. Sankar, S. Moran, P. A. Mazzali, J. Duarte, I. Salmaso, J. P. Anderson, C. Ashall, S. Benetti, M. Gromadzki, C. P. Gutiérrez, C. Humina, C. Inserra, E. Kankare, T. Kravtsov, T. E. Muller-Bravo, P. J. Pessi, J. Sollerman, D. R. Young, K. Chambers, T. de Boer, H. Gao, M. Huber, C. C. Lin, T. Lowe, E. Magnier, P. Minguez, I. A. Smith, K. W. Smith, S. Srivastav, R. Wainscoat, and M. Benedet. SN 2024abfo: A partially stripped type II supernova from a yellow supergiant. , 698:A129, June 2025. doi: 10.1051/0004-6361/202554388.

Jacco Vink. Evidence for Non-thermal Bremsstrahlung from the Supernova Remnant MSH14-63/RCW 86. In *Chandra Fellows Symposium 2001*, page 13, October 2001.

J. A. J. Alford, G. B. Zhang, and J. D. Gelfand. NuSTAR and XMM-Newton Observations of PSR J1930+1852 and Its Pulsar Wind Nebula. , 987(1):63, July 2025. doi: 10.3847/1538-4357/add92e.

M. G. Watson, J.-L. Augueres, J. Ballet, X. Barcons, D. Barret, M. Boer, T. Boller, G. E. Bromage, H. Brunner, F. J. Carrera, M. S. Cropper, M. Denby, M. Ehle, M. Elvis, A. C. Fabian, M. J. Freyberg, P. Guillout, J.-M. Hameury, G. Hasinger, D. A. Hinshaw, T. Maccacaro, K. O. Mason, R. G. McMahon, L. Michel, L. Mirioni, J. P. Mittaz, C. Motch, J.-F. Olive, J. P. Osborne, C. G. Page, M. Pakull, B. H. Perry, M. Pierre, W. Pietsch, J. P. Pye, A. M. Read, T. P. Roberts, S. R. Rosen, J.-L. Sauvageot, A. D. Schwope, K. Sekiguchi, G. C. Stewart, I. Stewart, I. Valtchanov, M. J. Ward, R. S. Warwick, R. G. West, N. E. White, and D. M. Worrall. The xmm-newton serendipitous survey. i. the role of xmm-newton survey science centre. *Astronomy & Astrophysics*, 365:L51–L59, January 2001. doi: 10.1051/0004-6361:20000067.

ESA: XMM-Newton SOC. *XMM-Newton Users Handbook*. European Space Agency, 2013. URL https://xmm-tools.cosmos.esa.int/external/xmm_user_support/documentation/uhb/. Prepared by the XMM-Newton Community Support Team.

European Space Agency. Radiators attached to the epic and rgs instruments passively cool the ccds to mitigate radiation-induced noise. https://arxiv.org/pdf/1202.1651, 2012. EPIC MOS-CCDs operate at approximately $-120°$C and the pn-CCD at similar low temperatures.

S. Snowden, Snowden @nasa, Steven, Gov, and K. Kuntz. Cookbook for analysis procedures for xmm-newton epic mos observations of extended objects and the diffuse background. *Version*, 43, 04 2011.

K. A. Arnaud. XSPEC: The First Ten Years. In George H. Jacoby and Jeannette Barnes, editors, *Astronomical Data Analysis Software and Systems V*, volume 101 of *Astronomical Society of the Pacific Conference Series*, page 17, January 1996.

P. Predehl, R. Andritschke, V. Arefiev, V. Babyshkin, O. Batanov, W. Becker, H. Böhringer, A. Bogomolov, T. Boller, K. Borm, W. Bornemann, H. Bräuninger, M. Brüggen, H. Brunner, M. Brusa, E. Bulbul, M. Buntov, V. Burwitz, W. Burkert, N. Clerc, E. Churazov, D. Coutinho, T. Dauser, K. Dennerl, V. Doroshenko, J. Eder, V. Emberger, T. Eraerds, A. Finoguenov, M. Freyberg, P. Friedrich, S. Friedrich, M. Fürmetz, A. Georgakakis, M. Gilfanov, S. Granato, C. Grossberger, A. Gueguen, P. Gureev, F. Haberl, O. Hälker,

G. Hartner, G. Hasinger, H. Huber, L. Ji, A. v. Kienlin, W. Kink, F. Korotkov, I. Kreykenbohm, G. Lamer, I. Lomakin, I. Lapshov, T. Liu, C. Maitra, N. Meidinger, B. Menz, A. Merloni, T. Mernik, B. Mican, J. Mohr, S. Müller, K. Nandra, V. Nazarov, F. Pacaud, M. Pavlinsky, E. Perinati, E. Pfeffermann, D. Pietschner, M. E. Ramos-Ceja, A. Rau, J. Reiffers, T. H. Reiprich, J. Robrade, M. Salvato, J. Sanders, A. Santangelo, M. Sasaki, H. Scheuerle, C. Schmid, J. Schmitt, A. Schwope, A. Shirshakov, M. Steinmetz, I. Stewart, L. Strüder, R. Sunyaev, C. Tenzer, L. Tiedemann, J. Trümper, V. Voron, P. Weber, J. Wilms, and V. Yaroshenko. The erosita x-ray telescope on srg. *Astronomy amp; Astrophysics*, 647:A1, February 2021. ISSN 1432-0746. doi: 10.1051/0004-6361/202039313. URL http://dx.doi.org/10.1051/0004-6361/202039313.

R. Sunyaev, V. Arefiev, V. Babyshkin, A. Bogomolov, K. Borisov, M. Buntov, H. Brunner, R. Burenin, E. Churazov, D. Coutinho, J. Eder, N. Eismont, M. Freyberg, M. Gilfanov, P. Gureyev, G. Hasinger, I. Khabibullin, V. Kolmykov, S. Komovkin, R. Krivonos, I. Lapshov, V. Levin, I. Lomakin, A. Lutovinov, P. Medvedev, A. Merloni, T. Mernik, E. Mikhailov, V. Molodtsov, P. Mzhelsky, S. Müller, K. Nandra, V. Nazarov, M. Pavlinsky, A. Poghodin, P. Predehl, J. Robrade, S. Sazonov, H. Scheuerle, A. Shirshakov, A. Tkachenko, and V. Voron. SRG X-ray orbital observatory. Its telescopes and first scientific results. , 656:A132, December 2021. doi: 10.1051/0004-6361/202141179.

Federico Zangrandi, Katharina Jurk, Manami Sasaki, Jonathan Knies, Miroslav D. Filipović, Frank Haberl, Patrick Kavanagh, Chandreyee Maitra, Pierre Maggi, Sara Saeedi, Dominic Bernreuther, Bärbel S. Koribalski, Sean Points, and Lister Staveley-Smith. First study of the supernova remnant population in the large magellanic cloud with erosita. *Astronomy and Astrophysics*, 692:A237, December 2024. ISSN 1432-0746. doi: 10.1051/0004-6361/202348868. URL http://dx.doi.org/10.1051/0004-6361/202348868.

R. C. Smith and MCELS Team. The UM/CTIO Magellanic Cloud Emission-line Survey. In Y. H. Chu, N. Suntzeff, J. Hesser, and D. Bohlender, editors, *New Views of the Magellanic Clouds*, volume 190 of *IAU Symposium*, page 28, January 1999.

Miroslav D Filipović, J L Payne, R Z E Alsaberi, R P Norris, P J Macgregor, L Rudnick, B S Koribalski, D Leahy, L Ducci, R Kothes, H Andernach, L Barnes, I S Bojičić, L M Bozzetto, R Brose, J D Collier, E J Crawford, R M Crocker, S Dai, T J Galvin, F Haberl, U Heber, T Hill, A M Hopkins, N Hurley-Walker, A Ingallinera, T Jarrett, P J Kavanagh, E Lenc, K J Luken, D Mackey, P Manojlović, P Maggi, C Maitra, C M Pennock, S Points, S Riggi, G Rowell, S Safi-Harb, H Sano, M Sasaki, S Shabala, J Stevens, J Th van Loon, N F H Tothill, G Umana, D Urošević, V Velović, T Vernstrom, J L West, and Z Wan. Mysterious odd radio circle near the large magellanic cloud – an intergalactic supernova remnant? *Monthly Notices of the Royal Astronomical Society*, 512(1): 265–284, 02 2022. ISSN 0035-8711. doi: 10.1093/mnras/stac210. URL https://doi.org/10.1093/mnras/stac210.

Tony Wong, Annie Hughes, Jürgen Ott, Erik Muller, Jorge L. Pineda, Jean-Philippe Bernard, You-Hua Chu, Yasuo Fukui, Robert A. Gruendl, Christian Henkel, Akiko Kawamura, Ulrich Klein, Leslie W. Looney, Sarah Maddison, Yoji Mizuno, Deborah Paradis, Jonathan Seale, and Daniel E. Welty.

The Magellanic Mopra Assessment (MAGMA). I. The Molecular Cloud Population of the Large Magellanic Cloud. , 197(2):16, December 2011. doi: 10.1088/0067-0049/197/2/16.

Tony Wong, Annie Hughes, Kazuki Tokuda, Rémy Indebetouw, Jean-Philippe Bernard, Toshikazu Onishi, Evan Wojciechowski, Jeffrey B. Bandurski, Akiko Kawamura, Julia Roman-Duval, Yixian Cao, C. H. Rosie Chen, You-hua Chu, Chaoyue Cui, Yasuo Fukui, Ludovic Montier, Erik Muller, Juergen Ott, Deborah Paradis, Jorge L. Pineda, Erik Rosolowsky, and Marta Sewiło. ALMA Observations of a Quiescent Molecular Cloud in the Large Magellanic Cloud. , 850(2):139, December 2017. doi: 10.3847/1538-4357/aa9333.

J. Koornneef. The gas to dust ratio and the near-infrared extinction law in the large magellanic cloud. *Astronomy and Astrophysics*, 107:247–251, 1982.

W. R. J. Rolleston, C. Trundle, and P. L. Dufton. The present-day chemical composition of the LMC. *Astronomy Astrophysics*, 396(1):53–64, 2002. doi: 10.1051/0004-6361:20021088.

R. A. Fesen, W. P. Blair, and R. P. Kirshner. Optical emission-line properties of evolved galactic supernova remnants. , 292:29–48, May 1985. doi: 10.1086/163130.

Maggi, P., Haberl, F., Kavanagh, P. J., Sasaki, M., Bozzetto, L. M., Filipović, M. D., Vasilopoulos, G., Pietsch, W., Points, S. D., Chu, Y.-H., Dickel, J., Ehle, M., Williams, R., and Greiner, J. The population of x-ray supernova remnants in the large magellanic cloud. *AA*, 585:A162, 2016. doi: 10.1051/0004-6361/201526932. URL https://doi.org/10.1051/0004-6361/201526932.

S. C. Russell and M. A. Dopita. Abundances of the heavy elements in the magellanic clouds. iii. *The Astrophysical Journal*, 384:508–522, 1992.

L. M. Bozzetto, P. J. Kavanagh, P. Maggi, M. D. Filipović, M. Stupar, Q. A. Parker, W. A. Reid, M. Sasaki, F. Haberl, D. Urošević, J. Dickel, R. Sturm, R. Williams, M. Ehle, R. Gruendl, Y. H. Chu, S. Points, and E. J. Crawford. Multifrequency study of a new Fe-rich supernova remnant in the Large Magellanic Cloud, MCSNR J0508-6902. , 439(1):1110–1124, March 2014. doi: 10.1093/mnras/stu051.

Luke M Bozzetto, Miroslav D Filipović, H Sano, R Z E Alsaberi, L A Barnes, I S Bojičić, R Brose, L Chomiuk, E J Crawford, S Dai, M Ghavam, F Haberl, T Hill, A M Hopkins, A Ingallinera, T Jarrett, P J Kavanagh, B S Koribalski, R Kothes, D Leahy, E Lenc, I Leonidaki, P Maggi, C Maitra, C Matthew, J L Payne, C M Pennock, S Points, W Reid, S Riggi, G Rowell, M Sasaki, S Safi-Harb, J Th van Loon, N F H Tothill, D Urošević, and F Zangrandi. New askap radio supernova remnants and candidates in the large magellanic cloud. *Monthly Notices of the Royal Astronomical Society*, 518(2):2574–2598, October 2022. ISSN 1365-2966. doi: 10.1093/mnras/stac2922. URL http://dx.doi.org/10.1093/mnras/stac2922.

Denis Leahy, Adam Foster, and Ivo Seitenzahl. On the interpretation of xspec abundances and emission measures, 2024. URL https://arxiv.org/abs/2311.11181.

Warth, Gabriele, Sasaki, Manami, Kavanagh, Patrick J., Filipović, Miroslav D., Points, Sean D., and Bozzetto, Luke M. Multi-frequency study of dem l299 in the large magellanic cloud. *AA*, 567:A136, 2014. doi: 10.1051/0004-6361/201423575. URL https://doi.org/10.1051/0004-6361/201423575.

Thomas G. Pannuti, Jeonghee Rho, Craig O. Heinke, and William P. Moffitt. The x-ray properties of five galactic supernova remnants detected by thespitzer-glimpse survey. *The Astronomical Journal*, 147(3):55, February 2014. ISSN 1538-3881. doi: 10.1088/0004-6256/147/3/55. URL http://dx.doi.org/10.1088/0004-6256/147/3/55.

D. S. Mathewson and V. L. Ford. HI surveys of the Magellanic system. In S. van den Bergh and K. S. D. de Boer, editors, *Structure and Evolution of the Magellanic Clouds*, volume 1983 of *IAU Symposium*, pages 125–136, September 1984. doi: 10.1017/S0074180900040092.

Sungeun Kim, Lister Staveley-Smith, Michael A. Dopita, Robert J. Sault, Kenneth C. Freeman, Youngung Lee, and You-Hua Chu. A neutral hydrogen survey of the large magellanic cloud: Aperture synthesis and multibeam data combined. *The Astrophysical Journal Supplement Series*, 148(2):473, oct 2003. doi: 10.1086/376980. URL https://dx.doi.org/10.1086/376980.

Sungeun Kim, Michael A. Dopita, Lister Staveley-Smith, and Michael S. Bessell. H i shells in the large magellanic cloud. *The Astronomical Journal*, 118(6):2797, dec 1999. doi: 10.1086/301116. URL https://dx.doi.org/10.1086/301116.

John Meaburn. The giant and supergiant shells of the Magellanic Clouds. *Monthly Notices of the Royal Astronomical Society*, 192(3):365–375, 10 1980. ISSN 0035-8711. doi: 10.1093/mnras/192.3.365. URL https://doi.org/10.1093/mnras/192.3.365.

Y. Fukui, A. Kawamura, T. Minamidani, Y. Mizuno, Y. Kanai, N. Mizuno, T. Onishi, Y. Yonekura, A. Mizuno, H. Ogawa, and M. Rubio. The second survey of the molecular clouds in the large magellanic cloud by nanten. i. catalog of molecular clouds. *The Astrophysical Journal Supplement Series*, 178 (1):56–70, September 2008. ISSN 1538-4365. doi: 10.1086/589833. URL http://dx.doi.org/10.1086/589833.

Jeonghee Rho and R. Petre. Mixed-morphology supernova remnants. *The Astrophysical Journal*, 503(2):L167, jul 1998. doi: 10.1086/311538. URL https://doi.org/10.1086/311538.

Patrick Slane, Andrei Bykov, Donald C. Ellison, Gloria Dubner, and Daniel Castro. *Supernova Remnants Interacting with Molecular Clouds: X-Ray and Gamma-Ray Signatures*, pages 187–210. Springer New York, New York, NY, 2016. ISBN 978-1-4939-3547-5. doi: 10.1007/978-1-4939-3547-5_6. URL https://doi.org/10.1007/978-1-4939-3547-5_6.

Charee L. Peters, Laura A. Lopez, Enrico Ramirez-Ruiz, Keivan G. Stassun, and Enectali Figueroa-Feliciano. Constraining Explosion Type of Young Supernova Remnants Using 24 μm Emission Morphology. , 771(2):L38, July 2013. doi: 10.1088/2041-8205/771/2/L38.

E. W. Pellegrini, M. S. Oey, P. F. Winkler, S. D. Points, R. C. Smith, A. E. Jaskot, and J. Zastrow. The optical depth of h ii regions in the magellanic clouds. *The Astrophysical Journal*, 755(1):40, July 2012. ISSN 1538-4357. doi: 10.1088/0004-637x/755/1/40. URL http://dx.doi.org/10.1088/0004-637X/755/1/40.

Dennis Zaritsky, Jason Harris, Ian B. Thompson, and Eva K. Grebel. The magellanic clouds photometric survey: The large magellanic cloud stellar catalog and extinction map. *The Astronomical Journal*, 128(4):1606, oct 2004. doi: 10.1086/423910. URL https://dx.doi.org/10.1086/423910.

A. Dotter. MESA Isochrones and Stellar Tracks (MIST) 0: Methods for the construction of stellar isochrones. *The Astrophysical Journal Supplement Series*, 222:8, 2016. URL https://www.researchgate.net/publication/290480424_MESA_Isochrones_and_Stellar_Tracks_MIST_0_Methods_for_the_construction_of_stellar_isochrones.

J. Choi, A. Dotter, C. Conroy, M. Cantiello, B. Paxton, and B. D. Johnson. MESA Isochrones and Stellar Tracks (MIST). I: Solar-Scaled Models. *The Astrophysical Journal*, 823:102, 2016. doi: 10.3847/0004-637X/823/2/102. URL https://arxiv.org/abs/1604.08592.

Bill Paxton, Lars Bildsten, Aaron Dotter, Falk Herwig, Pierre Lesaffre, and Frank Timmes. Modules for Experiments in Stellar Astrophysics (MESA). , 192(1):3, January 2011. doi: 10.1088/0067-0049/192/1/3.

Bill Paxton, Matteo Cantiello, Phil Arras, Lars Bildsten, Edward F. Brown, Aaron Dotter, Christopher Mankovich, M. H. Montgomery, Dennis Stello, F. X. Timmes, and Richard Townsend. Modules for Experiments in Stellar Astrophysics (MESA): Planets, Oscillations, Rotation, and Massive Stars. , 208(1):4, September 2013. doi: 10.1088/0067-0049/208/1/4.

Bill Paxton, Pablo Marchant, Josiah Schwab, Evan B. Bauer, Lars Bildsten, Matteo Cantiello, Luc Dessart, R. Farmer, H. Hu, N. Langer, R. H. D. Townsend, Dean M. Townsley, and F. X. Timmes. Modules for Experiments in Stellar Astrophysics (MESA): Binaries, Pulsations, and Explosions. , 220(1):15, September 2015. doi: 10.1088/0067-0049/220/1/15.

Edwin E. Salpeter. The Luminosity Function and Stellar Evolution. , 121:161, January 1955. doi: 10.1086/145971.

L. Woltjer. Supernova Remnants. , 10:129, January 1972. doi: 10.1146/annurev.aa.10.090172.001021.

Nari Suzuki, Shigeo Yamauchi, Kumiko K. Nobukawa, Masayoshi Nobukawa, and Satoru Katsuda. Detection of the neutral iron line from the supernova remnant W 49 B with Suzaku. , 76(2):265–271, April 2024. doi: 10.1093/pasj/psae006.

Tomomi Morikawa, Kumiko K Nobukawa, Shigetaka Saji, Hidetoshi Sano, Koharu Hirano, Masayoshi Nobukawa, Shigeo Yamauchi, Hideki Uchiyama, and Hironori Matsumoto. Non-thermal neutral iron line emission in the supernova remnants g304.6+0.1 and g346.6-0.2 interacting with molecular clouds. *Publications of the Astronomical Society of Japan*, 77(3):607–615, 04 2025. ISSN 2053-051X. doi: 10.1093/pasj/psaf027. URL https://doi.org/10.1093/pasj/psaf027.

F. Yusef-Zadeh, M. Wardle, J. Rho, and M. Sakano. Oh (1720 mhz) masers and mixed-morphology supernova remnants. *The Astrophysical Journal*, 585(1):319–323, March 2003. ISSN 1538-4357. doi: 10.1086/345932. URL http://dx.doi.org/10.1086/345932.

Acknowledgments

I acknowledge the guidance and support of Prof. Dr. Manami Sasaki throughout the working period on this thesis. The primary X-ray data analysed in this thesis was obtained by Dr. Sasaki.

I am grateful to Federico Zangrandi for his helps and inputs in every stage of this research. The inputs and helps by Sara Saeedi, Roman Laktionov, Martin Mayer, Mar Canal i Saguer and Vaibhav Shukla were also helpful. Their insights, along with the support of all the well-wishing scientists at the Remeis Observatory, made completing this thesis significantly easier.

Above all, I thank my father who has been my best star; without him, this fulfillment would have been impossible.

This research has made use of the software provided by the High Energy Astrophysics Science Archive Research Center (HEASARC), which is a service of the Astrophysics Science Division at NASA/GSFC.

Declaration

I, Edwin John Anthikat, student registration number: 23266993, hereby confirm that I completed the submitted work independently and without the unauthorized assistance of third parties and without the use of undisclosed and, in particular, unauthorized aids. This work has not been previously submitted in its current form or in a similar form to any other examination authorities and has not been accepted as part of an examination by any other examination authority.

Where the wording has been taken from other people's work or ideas, this has been properly acknowledged and referenced. This also applies to drawings, sketches, diagrams and sources from the Internet.

In particular, I am aware that the use of artificial intelligence is forbidden unless its use an aid has been expressly permitted by the examiner. This applies in particular to chatbots (especially ChatGPT) and such programs in general that can complete the tasks of the examination or parts thereof on my behalf.

Furthermore, I am aware that working with others in one room or by means of social media represents the unauthorized assistance of third parties within the above meaning, if group work is not expressly permitted. Each exchange of information with others during the examination, with the exception of examiners and invigilators, about the structure or contents of the examination or any other information such as sources is not permitted. The same applies to attempts to do so.

Any infringements of the above rules constitute fraud or attempted fraud and shall lead to the examination being graded "fail" ("nicht bestanden").

Erlangen, 14.01.2026

Edwin John Anthikat